A&A 581, A105 (2015)
DOI: 10.1051/0004-6361/201425128
© ESO 2015

Astronomy & Astrophysics

Planck's dusty GEMS: The brightest gravitationally lensed galaxies discovered with the *Planck* all-sky survey⋆

R. Cañameras[1,2], N. P. H. Nesvadba[2,1,⋆⋆], D. Guery[1,2], T. McKenzie[4], S. König[5], G. Petitpas[6], H. Dole[1,2,3], B. Frye[7], I. Flores-Cacho[8,9], L. Montier[8,9], M. Negrello[10], A. Beelen[1,2], F. Boone[9,10], D. Dicken[1,2,11], G. Lagache[1,2,12], E. Le Floc'h[11], B. Altieri[13], M. Béthermin[14], R. Chary[15], G. de Zotti[10], M. Giard[8,9], R. Kneissl[16,17], M. Krips[5], S. Malhotra[18], C. Martinache[1,2], A. Omont[19], E. Pointecouteau[8,9], J.-L. Puget[2,1], D. Scott[4], G. Soucail[8,9], I. Valtchanov[13], N. Welikala[20], and L. Yan[13]

(Affiliations can be found after the references)

Received 8 October 2014 / Accepted 5 June 2015

ABSTRACT

We present an analysis of CO spectroscopy and infrared-to-millimetre dust photometry of 11 exceptionally bright far-infrared (FIR) and sub-mm sources discovered through a combination of the *Planck* all-sky survey and follow-up *Herschel-SPIRE* imaging – "*Planck*'s Dusty Gravitationally Enhanced subMillimetre Sources". Each source has a secure spectroscopic redshift $z = 2.2$–3.6 from multiple lines obtained through a blind redshift search with EMIR at the IRAM 30-m telescope. Interferometry was obtained at IRAM and the SMA, and along with optical/near-infrared imaging obtained at the CFHT and the VLT reveal morphologies consistent with strongly gravitationally lensed sources, including several giant arcs. Additional photometry was obtained with JCMT/SCUBA-2 and IRAM/GISMO at 850 μm and 2 mm, respectively. The SEDs of our sources peak near either the 350 μm or 500 μm bands of SPIRE with peak flux densities between 0.35 and 1.14 Jy. All objects are extremely bright isolated point sources in the 18″ beam of SPIRE at 250 μm, with apparent FIR luminosities of up to $3 \times 10^{14}\,L_{\odot}$ (not correcting for the lensing effect). Their morphologies, sizes, CO line widths, CO luminosities, dust temperatures, and FIR luminosities provide additional empirical evidence that these are amongst the brightest strongly gravitationally lensed high-redshift galaxies on the sub-mm sky. Our programme extends the successful wide-area searches for strongly gravitationally lensed high-redshift galaxies (carried out with the South Pole Telescope and *Herschel*) towards even brighter sources, which are so rare that their systematic identification requires a genuine all-sky survey like *Planck*. Six sources are above the ≃600 mJy 90% completeness limit of the *Planck* catalogue of compact sources (PCCS) at 545 and 857 GHz, which implies that these must literally be amongst the brightest high-redshift FIR and sub-mm sources on the extragalactic sky. We discuss their dust masses and temperatures, and use additional WISE 22-μm photometry and template fitting to rule out a significant contribution of AGN heating to the total infrared luminosity. Six sources are detected in FIRST at 1.4 GHz, and the others have sensitive upper limits. Four have flux densities brighter than expected from the local FIR-radio correlation, but in the range previously found for high-z sub-mm galaxies, one has a deficit of FIR emission, and 6 are consistent with the local correlation, although this includes 3 galaxies with upper limits. We attribute this to the turbulent interstellar medium of these galaxies, rather than the presence of radio AGN. The global dust-to-gas ratios and star-formation efficiencies of our sources are predominantly in the range expected from massive, metal-rich, intense, high-redshift starbursts. An extensive multi-wavelength follow-up programme is being carried out to further characterize these sources and the intense star formation within them.

Key words. galaxies: high-redshift – galaxies: star formation – galaxies: starburst – submillimeter: galaxies – gravitational lensing: strong – galaxies: formation

1. Introduction

The brightest, most strongly gravitationally lensed galaxies in the high-redshift Universe have an extraordinary potential to advance our understanding of the processes that regulate the growth of the most massive galaxies we see today. In particularly fortuitous cases, gravitational lensing from massive, intervening galaxies, or galaxy clusters not only boosts the apparent integrated brightness of high-redshift galaxies by factors up to 20–60, but also magnifies their images by similar factors while conserving surface brightness. Thereby, they allow us to study the fine spatial details of intensely star-forming high-redshift galaxies at scales much below 1 kpc, down to around 100 pc (e.g., Swinbank et al. 2010, 2011). This is more akin to the scales of individual star-forming regions in nearby galaxies than the galaxy-wide scales (of order a few kpc) with which we must otherwise content ourselves at cosmological distances.

Since the discovery of the first gravitationally lensed galaxy in the optical (Soucail et al. 1987; the first gravitationally lensed quasar had already been discovered by Walsh et al. 1979), strongly gravitationally lensed galaxies have been identified and studied in all wavebands from the ground and in space. Strongly gravitationally lensed sub-mm galaxies provide an extraordinary possibility to probe individual star-forming regions in the most intensely star-forming high-redshift galaxies. They are also very promising sources for increasing our understanding of how the deep gravitational potential well of high-redshift galaxies, their high gas fractions and gas-mass surface densities, and feedback from star formation and perhaps active galactic nuclei (AGNs) are setting the stage for the intense star formation at fine spatial

⋆ Based on observations collected with the *Herschel* and *Planck* satellites, IRAM, SMA, JCMT, CFHT, and the VLT.

⋆⋆ Corresponding author: N. Nesvadba,
e-mail: nicole.nesvadba@ias.u-psud.fr

detail (e.g., Danielson et al. 2011; Swinbank et al. 2011; Combes et al. 2012).

Massive, dust-enshrouded and relatively evolved high-redshift galaxies are characterized by the bright thermal infrared emission from dust heated by intense star formation during their rapid primordial growth phase. These galaxies have typical stellar and dynamical masses of a few times $10^{10-11}\,M_{\odot}$ (Smail et al. 2004; Swinbank et al. 2006; Nesvadba et al. 2007) and form stars at prodigious rates of up to about $1000\,M_{\odot}\,\mathrm{yr}^{-1}$, which are unparallelled in the nearby Universe. As a population, dusty starburst galaxies may have contributed as much as about half of the total energy production from star formation at these cosmic epochs (e.g., Hauser & Dwek 2001; Dole et al. 2006).

Unfortunately, given their importance for our understanding of high-redshift star formation and galaxy growth, the high stellar and dynamical masses and short evolutionary timescales of these galaxies make them very rare on the sky. The densities of far-infrared (FIR) and submillimetre (sub-mm) selected galaxies that are bright enough to be good candidates for strong gravitational lensing are only around one every few square degrees for sources with $S_{500} \approx 100$ mJy, with large uncertainties. For example, Lapi et al. (2012) predict about 0.003–0.1 deg^{-2} for sources with $S_{500} \geq 400$ mJy on the sky, for expected maximum gravitational magnification factors of 20–30 adopted in the models. Consequently, we may expect to find only a few of these sources on the entire extragalactic sky, in accordance with models of the diffuse infrared background light (Béthermin et al. 2012). Nonetheless, at luminosities above about $10^{13}\,L_{\odot}$ (corresponding to $S_{500} \approx 100$ mJy), they are expected to dominate the integrated FIR and sub-mm luminosity function (Negrello et al. 2007).

A major breakthrough has been the recent discovery by *Herschel*[1] and the South-Pole Telescope (SPT) of sizeable sets of strongly gravitationally lensed submillimetre galaxies, with typical magnification factors of a few. These are using the new generation of wide-field surveys (several thousand square degrees), probing in particular the range in FIR and sub-mm flux density between 100 and 200 mJy (e.g., Negrello et al. 2010; Harris et al. 2012; Vieira et al. 2013; Wardlow et al. 2013; Bussmann et al. 2013). Most gravitationally lensed sources identified in these surveys are magnified by individual massive galaxies at intermediate redshifts, producing partial Einstein rings of a few arcsec in diameter and magnification factors up to about 10. However, the number of sources identified in these surveys above flux densities of 200–300 mJy remains rather small. For example, Bussmann et al. (2013) list 30 sources with FIR fluxes in this range, with six sources above $S_{350} = 350$ mJy. So far, to our knowledge only one source with $S_{350} > 500$ mJy at 350 μm has been published by the SPT collaboration (Vieira et al. 2013). Meanwhile, the brightest source in the Bussmann et al. (2013) sample has $S_{350} = 484$ mJy.

The extragalactic *Herschel* and SPT surveys together cover about 4% of the sky, which highlights the importance of having an all-sky survey to identify high-redshift FIR and sub-mm galaxies above the 100–300 mJy regime in a systematic way. These sources are likely to be amongst the most strongly gravitationally lensed galaxies on the sky. *Planck* is the first all-sky survey in the submillimetre with the depth and spatial resolution necessary to probe the brightest, and presumably most strongly gravitationally lensed high-redshift infrared galaxies observable to us. The 90% completeness limit of the *Planck* Catalogue of Compact Sources (PCCS) corresponds to $L_{\mathrm{IR}} \approx 6 \times 10^{13}\,L_{\odot}$ at $z = 2$ (Planck Collaboration XXVIII 2014). At these luminosities, even all-sky surveys may reveal only few sources (Negrello et al. 2010; Béthermin et al. 2012; Lapi et al. 2012). For example, Herranz et al. (2013) find only very few high-redshift sources in the Early Release Catalogue of Compact Sources (ERCSC) from *Planck* (Planck Collaboration VII 2011), primarily blazars. Most extragalactic sources in the ERCSC are low-redshift galaxies.

We used photometry derived from *Planck*-HFI (described in Planck Collaboration I 2014; Planck Collaboration VI 2014) to identify all compact sources in the *Planck* maps that have colours consistent with being exceptionally bright, dusty, intensely star-forming high-redshift galaxies. We then obtained FIR photometry of the most promising candidates (the "HPASSS" programme, Planck Collaboration Int. XXVII 2015, hereafter Paper I), using the Spectral and Photometric Imaging Receiver (SPIRE) on-board the *Herschel* space telescope. This sample, obtained through *Herschel* "Must-Do" Director's Discretionary Time, includes 234 of the brightest, rarest sources in the sky (one source per several tens of square degrees, Planck Collaboration, in prep.). The sample was deliberately selected to only include sources that do not fall into the large *Herschel* survey fields, and which are new to the literature. SPIRE confirms that these sources have the typical sub-mm colours of high-z infrared and sub-mm galaxies. Most of the 234 sources of the HPASSS sample are overdensities of multiple galaxies with the typical FIR colours of high-z galaxies, and only four are Galactic cirrus clouds. Another small subset are bright individual, isolated point sources in the 20″ beam of SPIRE, consistent with being exceptionally bright, presumably strongly gravitationally lensed high-redshift galaxies. An overview of the HPASSS sample is given in Paper I.

Here we present the first results of our multi-wavelength follow-up of the 11 brightest of these isolated HPASSS sources ("*Planck*'s Dusty GEMS"), which can be observed from the northern hemisphere. All have flux densities at 350 μm measured with SPIRE that are at least $S_{350} \approx 300$ mJy, well above the typical range probed by the SPT and wide-field *Herschel* surveys. The brightest source has $S_{350} = 1050$ mJy. Welikala et al. (2015) discuss another set of weaker gravitational lenses observed with *Planck* and the SPT; however, the 11 sources we discuss here were previously unknown and are substantially brighter. Another source, PLCKERC857 PLCK_G270.59+58.52, taken from the ERCSC, which also satisfies our selection criteria and fortuitously falls into the H-ATLAS survey area, has already been discussed by Fu et al. (2012), Herranz et al. (2013), and Bussmann et al. (2013). HLS 091828.6+514223 at $z = 5.2$ (Combes et al. 2012; Rawle et al. 2014) behind the galaxy cluster Abell 773, has been discovered independently from our survey as part of the *Herschel* Lensing Survey (Egami et al. 2010), but is also included in our *Planck* parent sample (Paper I). It forms a 1.5″, near-complete Einstein ring with a magnification factor of 9 ± 2 (Rawle et al. 2014).

Our present analysis has three main goals. Firstly, we determine spectroscopic redshifts and provide empirical evidence from millimetre photometry and spectroscopy that these are indeed high-redshift sources, which owe their exceptional brightness in the submillimetre to strong gravitational lensing. We also show ground-based near-infrared (NIR) imaging, illustrating that the sub-mm sources lie behind overdense regions in the intermediate-redshift Universe. Secondly, we characterize their global dust and star-formation properties and show that their observed FIR emission is dominated by star formation, not by

[1] *Herschel* is an ESA space observatory with science instruments provided by European-led Principal Investigator consortia and with important participation from NASA.

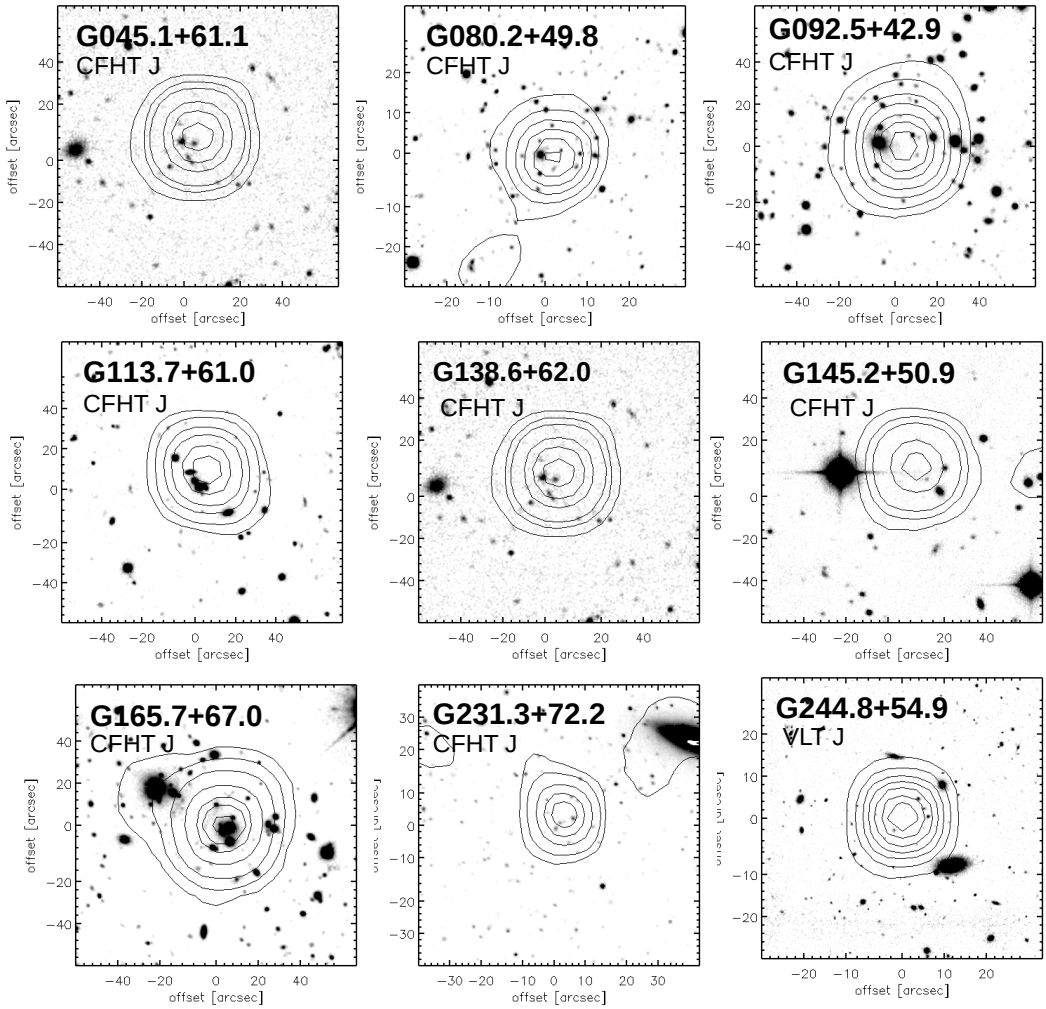

Fig. 1. Near-infrared *J*-band images of the nine sources for which we already have optical/NIR imaging and millimetre interferometry (Fig. 2). Contours show the *Herschel-SPIRE* morphology at 250 μm.

powerful obscured quasars. Thirdly, we estimate molecular gas masses from their CO line emission, calculate dust-to-gas mass ratios, and use their FIR luminosities and molecular gas mass estimates to show that they are more akin to very rapidly forming "starburst" galaxies, than the more gradually, but still intensely star-forming high-redshift galaxies on the "main sequence" (e.g., Elbaz et al. 2011). This is the first in a series of papers about "Planck's Dusty GEMS", and for this analysis we only use parts of the comprehensive data sets we already have in hand. Subsequent publications will provide lensing model solutions, discuss the spatially-resolved properties of our sources in a number of wavebands, and use the multiple millimetre line detections to investigate the detailed gas and star-formation properties of these systems.

The outline of the paper is as follows. After the descriptions of our sample selection in Sect. 2, and our follow-up observations and data reduction in Sect. 3, we provide the redshifts in Sect. 4.2, and the FIR luminosities, dust masses and temperatures in Sect. 5. In Sect. 6 we present the evidence that our sources are very strongly gravitationally lensed galaxies, including arcsec-resolution sub-mm and millimetre interferometry of the dust emission, as well as NIR/optical imaging. In Sect. 7 we impose additional constraints from the *Wide*-field Infrared Survey Explorer, WISE and the VLA FIRST survey to demonstrate that the FIR spectral energy distributions (SEDs) of our sources are not dominated by radiation from powerful AGN, before turning to their gas and star-formation properties in Sects. 9 and 10, respectively. We summarize our results in Sect. 11. Throughout the paper we adopt a flat $H_0 = 70\,\mathrm{km\,s^{-1}\,Mpc^{-1}}$ concordance cosmology with $\Omega_\mathrm{M} = 0.3$ and $\Omega_\Lambda = 0.7$.

2. Sample selection

In Fig. 1 we show 9 of our 11 newly discovered gravitational lens candidates, which are the brightest amongst our sources selected from the nominal data release of the *Planck* all-sky survey. The parent sample consists of two subsets that were identified with similar colour cuts in the 857-GHz to 545-GHz flux density ratio of $S_{857}/S_{545} < 1.5$–2. This is well-matched to the expected spectral shape of the FIR continuum of dusty starburst galaxies at redshifts $z \gtrsim 2$. Six of our sources were taken from the PCCS, which includes all sources with $S/N > 4$ at 545 GHz on the cleanest 52% of the sky (Planck Collaboration XXVIII 2014). Five sources come from a dedicated, blind search for high-redshift candidates in the *Planck* maps, which probes fainter sources in the cleanest 35% of the sky after subtracting estimates of the cosmic microwave background and Galactic cirrus emission. Table 1 lists the origin

Table 1. Mid-IR to millimetre photometry.

Source	Survey	RA (J2000)	Dec (J2000)	z_{source}	$z_{fg,sdss}$	S_{22} [mJy]	S_{250} [mJy]	S_{350} [mJy]	S_{500} [mJy]	S_{850} [mJy]	S_{2000} [mJy]
PLCK_G045.1+61.1 . .	OT2	15:02:36.04	+29:20:51	3.4	0.56[a,b]	<5.4	161 ± 5	328 ± 6	397 ± 6	130 ± 13	13 ± 2
PLCK_G080.2+49.8 . .	OT2	15:44:32.40	+50:23:46	2.6	0.5	<5.4	220 ± 9	340 ± 6	314 ± 6	87 ± 5	7 ± 2
PLCK_G092.5+42.9 . .	PCCS	16:09:17.76	+60:45:21	3.3	0.5	<5.4	765 ± 7	865 ± 8	696 ± 7	191 ± 16	8.4 ± 0.6
PLCK_G102.1+53.6 . .	OT2	14:29:17.98	+59:21:09	2.9	0.74[a]	8.1 ± 0.7	327 ± 4	410 ± 5	339 ± 5	. . .	5.5 ± 0.7
PLCK_G113.7+61.0 . .	PCCS	13:23:02.88	+55:36:01	2.4	0.3	6.0 ± 0.7	672 ± 7	603 ± 6	373 ± 5	108 ± 10	4 ±1
PLCK_G138.6+62.0 . .	PCCS	12:02:07.68	+53:34:40	2.4	0.4	6.2 ± 0.8	619 ± 6	664 ± 8	474 ± 6	123 ± 14	7 ±1
PLCK_G145.2+50.9 . .	PCCS	10:53:22.56	+60:51:49	3.6	. . .	<5.4	453 ± 5	719 ± 7	781 ± 8	360 ± 23	38 ±4
PLCK_G165.7+67.0 . .	PCCS	11:27:14.60	+42:28:25	2.2	0.34[a,b]	10.4 ± 0.9	867 ± 8	753 ± 6	472 ± 5	90 ± 9	8 ±1
PLCK_G200.6+46.1 . .	OT2	09:32:23.67	+27:25:00	3.0	0.6	<5.4	209 ± 4	294 ± 4	273 ± 5	110 ± 10	7 ±2
PLCK_G231.3+72.2 . .	OT2	11:39:21.60	+20:24:53	2.9	0.1	<5.4	299 ± 4	401 ± 5	341 ± 6	111 ± 12	9 ± 1
PLCK_G244.8+54.9 . .	PCCS	10:53:53.04	+05:56:21	3.0	0.13	<5.4	1050 ± 10	1054 ± 10	777 ± 7	198 ± 11	19 ± 2
HLS-J0918[c]		09:18:28.6	+51:42:23	5.2			85 ± 8	168 ± 8	203 ± 9	125 ± 8	15 ± 7
HATLAS-J1146[d]		11:46:37.9	−00:11:32	3.3			323 ± 24	378 ± 28	298 ± 24	93 ± 12	38 ± 6

Notes. The columns are: source name; indication of whether the sources come from the PCCS or our own high-z selection (OT2, see Sect. 2); RA and Dec coordinates; redshift of the high-z source; SDSS redshift of the intervening foreground source; WISE 22-μm flux density; *Herschel-SPIRE* 250-μm flux density; *Herschel-SPIRE* 350-μm flux density; *Herschel-SPIRE* 500-μm flux density; JCMT/SCUBA-2 850-μm flux density; and IRAM 30-m/GISMO 2-mm flux density. [(a)] Spectroscopic redshift of intervening foreground source from the SDSS. [(b)] Multiple foreground sources at a common spectroscopic redshift near the line of sight. [(c)] This source has been found with the *Herschel* Lensing Survey and has previously been discussed by Combes et al. (2012) and Rawle et al. (2014). The last column lists the 1.2-mm flux density measured with MAMBO on the IRAM 30-m telescope. [(d)] This source from the ERCSC (Planck Collaboration VII 2011) falls serendipitously into the HATLAS field and has been previously discussed by Fu et al. (2012). The last column lists the 1.2-mm flux density measured with MAMBO on the IRAM 30-m telescope.

of each target. The second subsample will be described in detail by Planck Collaboration (in prep.). A comprehensive summary of the selection and in particular the cleaning algorithm adopted to identify this subsample is given in Paper I.

All sources were followed up with *Herschel-SPIRE* photometry at 250 μm, 350 μm, and 500 μm as part of the HPASSS survey, mostly during "Must-Do" Director's Discretionary Time, and is a subset of the sample presented in Paper I. SPIRE has about 10 times greater depth and 20 times higher spatial resolution than *Planck*, with beam FWHMs of 18″, 24″, and 35″ at 250 μm, 350 μm, and 500 μm, respectively[2]. Therefore, SPIRE can be used to identify and localize the counterparts of *Planck* sources in the same wavelength regime. We identified all potential gravitationally lensed galaxies as bright, isolated point sources in the SPIRE images, with SEDs peaking at flux densities above 300 mJy in either the 350 μm or the 500 μm band as observed with SPIRE (in the final calibration of our SPIRE maps, one source has S_{350} = 294 mJy). This is well matched to the 90% completeness limit of the PCCS of about 600 mJy (Planck Collaboration XXVIII 2014), and purposefully excludes similar sources already identified in other surveys.

We find a total of 15 gravitational lens candidates. For the purposes of this paper, we exclude the two already described in the literature (Fu et al. 2012; Combes et al. 2012, see Sect. 1), and another two that are in the far South. The source described by Combes et al. (2012) is at a higher redshift (z = 5.2) than the sources we discuss here. Apart from that, including those other sources would not change our general conclusions.

In the present analysis we discuss the 11 Northern sources that are already spectroscopically confirmed to be at high redshifts. It is worth noting that by focusing on single, very bright sources in the *Herschel* images, we may have missed sets of multiple, but fainter gravitationally lensed objects behind the same intervening structures; these we would have identified as overdensities of high-redshift infrared galaxies in the overall HPASSS sample (Paper I). Irrespective of this, given the extraordinary sky coverage of our parent sample and the brightness of our targets, six of which reach or even exceed the completeness limits of the PCCS in the 353, 545, and 857 GHz bands of 330, 570, and 680 mJy, respectively (Table 1 of Planck Collaboration XXVIII 2014), the 11 sources discussed here are likely to be amongst the brightest individual high-redshift galaxies on the sky.

3. Photometry

3.1. Herschel-SPIRE FIR photometry

We base our analysis on the *Herschel-SPIRE* photometry at 250 μm, 350 μm, and 500 μm, as well as on ground-based JCMT/SCUBA-2 850-μm and IRAM/GISMO 2-mm single-dish photometry. For sources in the range z = 2.2–3.6, this corresponds to a wavelength range 50–80 μm and 400–600 μm in the rest-frame, which cover the expected peak and Rayleigh-Jeans tail, respectively, of the warm dust emission heated by intense star formation.

Herschel-SPIRE observations were carried out between December 2012 and March 2013. The *Herschel-SPIRE* photometry was obtained using `STARFINDER` (Diolaiti et al. 2000) as part of the HPASSS survey, and is discussed in detail in Paper I. `STARFINDER` integrates over the point spread function obtained directly from the image, and is therefore more suitable for data dominated by confusion noise than classical aperture photometry. Measured flux densities are between 294 mJy and 1054 mJy at 350 μm and between 270 mJy and 800 mJy at 500 μm, respectively (Table 1). Typical uncertainties are of the order of 5–10 mJy, which is close to the confusion level in the

[2] See the SPIRE Handbook 2014, `http://herschel.esac.esa.int/Docs/SPIRE/spire_handbook.pdf`

maps (Nguyen et al. 2010), but only includes the measurement error, not the systematic uncertainty of 7% inherent in the SPIRE photometry. However, this has no impact on our results.

3.2. JCMT/SCUBA-2 photometry at 850 μm

The SCUBA-2 (Holland et al. 2013) data were taken between September 2012 and May 2014 in moderate conditions with individual observing times of 15 min per source. The data were reduced using a configuration file optimized for point-source calibrators using the `smurf` data reduction software package for SCUBA-2 (Chapin et al. 2013). Flux densities were extracted using aperture photometry with a 30″ diameter aperture, where the background was estimated within an annulus with inner and outer diameters of 37.5″ and 60″, respectively. Uncertainties are between 4 mJy and 21 mJy per beam. These flux densities are then corrected for missing flux density due to the aperture size by dividing by 0.85, as described by Dempsey et al. (2013). An 8% calibration uncertainty is added in quadrature to the photometric errors. The resulting 850 μm flux densities are listed in Table 1.

3.3. SMA 850 μm interferometry

All sources were also observed in the continuum with the SMA in the 850 μm band. Observations were carried out between June 2013 and June 2014. Data were taken under good to excellent conditions with $pwv < 2$ mm in shared-track mode to obtain good uv coverage, in spite of observing each source with less than one track; this was made possible by their extraordinary brightness in the submillimetre. Integration times per source are between 2 and 7 h. All sources but PLCK_G080.2+49.8 were observed through programme 2013B-S050 in the compact configuration, with a beam of about 2″ × 2″. PLCK_G080.2+49.8 was observed through DDT programme 2013A-S075 in the extended configuration, giving a beam of 0.8″ × 0.5″. Data were calibrated in IDL using the `MIR` package, and analysis and imaging utilized the `MIRIAD` package. A full discussion of the interferometry is beyond the scope of the present analysis, and will be presented in a subsequent publication. Here we only use the 850 μm morphologies to illustrate that these are indeed strongly gravitationally lensed galaxies. Comparison with the single-dish flux densities from SCUBA-2 suggests that we recover at least 80–90% of the total flux density, implying that we have typically not missed fainter, more extended components.

3.4. IRAM-30-m /GISMO 2-mm photometry

Two-mm continuum observations were carried out with the 30-m telescope of IRAM between 17 and 23 April with 1.3–1.7 mm of precipitable water vapour, and between 29 October and 5 November 2013, with 3.4–8.6 mm of preciptable water vapour (programmes 222-12 and 100-13).

We used the 8 × 16 pixel bolometer camera GISMO, which covers a frequency range of 140–162 GHz (Staguhn et al. 2012) in the 2-mm band. At the 30-m telescope of IRAM, GISMO covers a 1.8′ × 3.7′ field of view with a 21″ × 21″ beam. We used 2′ × 2′ Lissajous maps with a relative flux density stability of about 8%, which is optimized to obtain high signal-to-noise ratios of relatively faint objects like ours, with only a small number of bad channels. Total integration times per source were between 10 and 100 min, depending on the expected flux density of the target.

We used the `CRUSH` software package (Kovacs 2013) to reduce and calibrate individual scans, and to combine them into the final image. We used the "faint" option, which is well adapted to signals around 10 mJy, detected at signal-to-noise ratios of less than 10 per scan. We detected all targets as point sources, with S/N between 3.4 and 14.8.

3.5. CFHT and VLT optical/NIR photometry

In order to identify and broadly characterize the foreground lensing structure, we also obtained NIR optical imaging of our sample using Megacam and WIRCAM on the Canada-France-Hawaii Telescope (CFHT), and with HAWKI and FORS on the Very Large Telescope (VLT) of the European Southern Observatory (ESO). Here we use the optical imaging to highlight that our sources lie behind massive intervening structures, either galaxy groups or clusters. Observations of the overall sample are still on-going, but have already provided us with optical or NIR imaging of all but one target in at least one band. We used the `scamp` and `swarp` software (Bertin 2010a,b) to register our images relative to the USNO-B2 catalog, with a typical positional uncertainty of 0.2″−0.5″. A full discussion of these data and what they imply more quantitatively for the lensing configuration will be presented in a subsequent publication.

4. Blind spectroscopic redshift survey in the millimetre

4.1. IRAM 30 m/EMIR spectroscopy

We performed a blind redshift search in the 3-mm and 2-mm bands for all 11 targets using the wide-band heterodyne receiver EMIR at the 30-m telescope of IRAM. Following a pilot programme to measure a spectroscopic redshift of our first source, PLCK_G080.2+49.8, through regular programme 82-12 and Director's Discretionary programme D05-12, we obtained another 75 h of observing time through Director's Discretionary programme D09-12 and the regular programme 094-13 in April and June 2013. For all sources we used the WILMA and FTS backends during good to variable conditions.

Individual scans were 30 s long, and we observed sets of 12 scans followed by a calibration. Data were reduced using `CLASS` (Gildas Team 2013). We took advantage of a dedicated routine kindly provided by C. Kramer to individually correct the baselines in each of the sub-bands of the FTS backend. The full set of lines will be discussed in a subsequent publication; here we only use the lowest-J CO transition available in each source, which provides additional empirical evidence that these are strongly gravitationally lensed galaxies. The redshifts are also derived from these lines, and found to be consistent with the full set of available lines per galaxy.

4.2. Spectroscopic redshifts

To obtain a spectroscopic redshift for each source, we started with a blind line search in the 3-mm atmospheric window, which we cover almost entirely with two interleaved tunings of EMIR centred at 89.4 GHz and 97.4 GHz, respectively. We used the WILMA and FTS backends in parallel, which have band widths of about 4 GHz and 8 GHz, respectively.

We discovered a bright emission line in each source in one of the tunings in the 3-mm band (Fig. 3). Subsequently we calculated all possible redshifts compatible with the observed frequency of the line, and tested our redshift hypothesis by

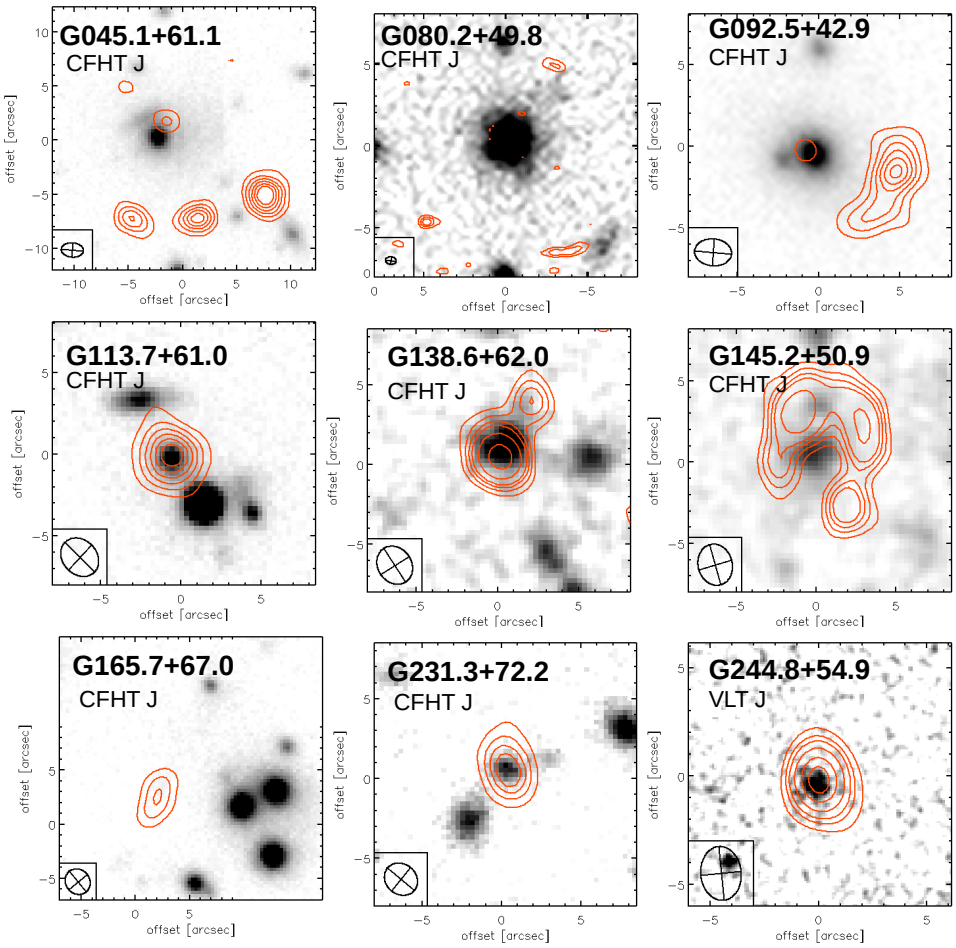

Fig. 2. Near-infrared J-band images of the nine sources from Fig. 1. Contours show the SMA morphology at 850 μm. The FWHM beam size of all SMA data is about 2″ (the FWHM beam size is shown in the bottom left corner of each panel), except for PLCK_G080.2+49.8, where it is 0.8″.

searching for a second line (typically CO(5–4) or CO(4–3)) at the predicted higher frequency. This required a separate frequency tuning, with the choice depending on each redshift hypothesis (typically lying in the 2-mm band). We started with the redshift that was closest to the photometric redshift derived from our SPIRE photometry, assuming a dust temperature of $T_{\rm d}$ = 30 K, which is the temperature of the dust component that dominates the FIR SED of the Cosmic Eyelash (Ivison et al. 2010b). This yielded the correct redshift in all but the two galaxies, specifically those with the highest dust temperatures (Table 2). In the end, our EMIR follow-up spectroscopy led to accurate and secure spectroscopic redshifts for all 11 targets, with 2–8 lines detected per source; this provides a wide range of constraints on the physical properties of the gas in these galaxies, which we will discuss in more detail in forthcoming papers.

Planck's Dusty GEMS fall in the redshift range of z = 2.2–3.6, comparable to that of radio-selected submillimetre galaxies in the field (Chapman et al. 2005), and very similar to that of gravitationally lensed sub-mm galaxies in the H-ATLAS survey (z = 2.1–3.5; Harris et al. 2012; Bussmann et al. 2013). The average redshift of *Planck*'s Dusty GEMS, z = 2.9 ± 0.4 (we give the width of the distribution here), is somewhat lower than the redshift range of the bright gravitationally lensed sub-mm galaxies from the SPT survey. The SPT sample has a mean redshift of z = 3.5, obtained from at least two lines for 12 of their 26 targets, and a combination of single-line detections and FIR photometric constraints for the remaining targets (Vieira et al. 2013; Weiß et al. 2013). One reason that we probe somewhat lower redshifts may be that we select our sources at shorter wavelengths (350–850 μm, compared to 1.4 and 2.0 mm for the SPT). However, we stress that our parent sample from *Planck* does include sources with higher redshifts, such as HLS 091828.6+514223 at z = 5.2 (Combes et al. 2012; Rawle et al. 2014), a source we selected independently from its confirmation as a high-z source through the HLS survey. We also note that the *Planck* selection is based on 350 μm, 550 μm, and 850 μm measurements, covering somewhat longer wavelengths than the blind *Herschel* surveys. The *Planck* high-z sample has a range of FIR colours, and the redshift distribution derived from the subsample of very bright gravitational lenses does not necessarily correspond to the redshift distribution of the overall *Planck* high-z sample (HLS 091828.6+514223 at z = 5.2 being a case in point).

4.3. Line profiles and luminosities

Figure 3 shows the lines we detected in the 3-mm band. Many sources exhibit complex line profiles, which can also be seen in the higher frequency data (Canameras et al., in prep.). These may either originate from several, gravitationally lensed regions in the same galaxy that are blended in the large (20″) beam of

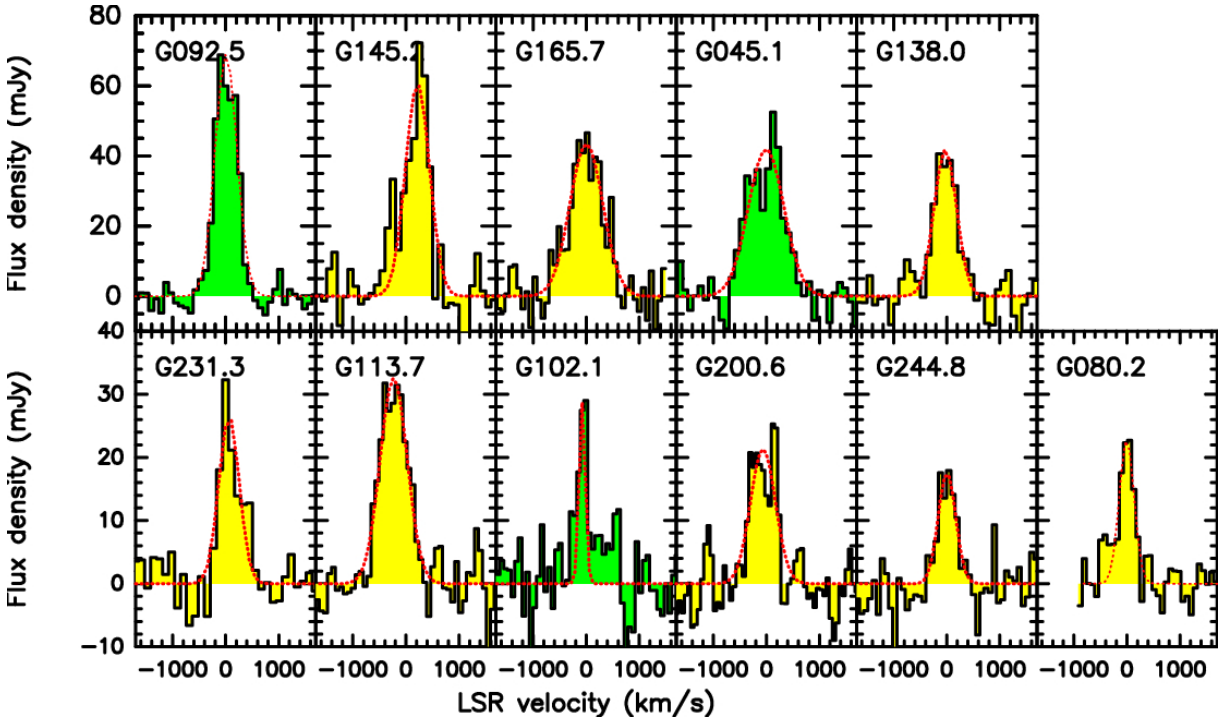

Fig. 3. Lowest-J CO emission line in each of our targets. CO(3–2) and CO(4–3) are indicated in yellow and green, respectively. Red dotted lines show simple single-Gaussian fits.

Table 2. Fitted parameters to the FIR dust continuum and dust properties.

Source	$\lambda_{\rm max}$	$S_{\rm max}$	$\mu\,L_{\rm FIR}$	$\mu\,L_{\rm FIR}^{\rm TPL}$	$\mu\,SFR$	$T_{\rm d}$	$\mu\,M_{\rm d}$	$L_{\rm FIR,AGN}/L_{\rm FIR,tot}$
	[μm]	[mJy]	[$10^{13}\,L_\odot$]	[$10^{13}\,L_\odot$]	[$M_\odot\,{\rm yr}^{-1}$]	[K]	[$10^9\,M_\odot$]	[%]
PLCK_G045.1+61.1	420 ± 10	360 ± 10	8.4 ± 0.1	12.1 ± 0.1	14 462 ± 172	36.0 ± 0.5	6.5 ± 0.1	
PLCK_G080.2+49.8	370 ± 10	345 ± 5	4.6 ± 0.1	7.1 ± 0.1	7920 ± 172	33.0 ± 0.5	7.2 ± 0.2	
PLCK_G092.5+42.9	322 ± 5	900 ± 10	24.8 ± 0.2	34.8 ± 0.2	42 698 ± 344	50.1 ± 0.4	5.3 ± 0.1	10
PLCK_G102.1+53.6	333 ± 4	410 ± 5	7.9 ± 0.1	11.9 ± 0.1	13 601 ± 172	41.1 ± 0.3	4.3 ± 0.1	
PLCK_G113.7+61.0	255 ± 20	700 ± 30	9.9 ± 0.2	12.6 ± 0.1	17 044 ± 344	45.0 ± 0.4	3.5 ± 0.1	
PLCK_G138.6+62.0	305 ± 10	690 ± 5	9.0 ± 0.1	13.5 ± 0.1	15 495 ± 172	38.7 ± 0.3	6.4 ± 0.1	
PLCK_G145.2+50.9	400 ± 10	785 ± 30	21.8 ± 0.2	30.1 ± 0.2	37 533 ± 344	40.5 ± 0.4	11.0 ± 0.1	33
PLCK_G165.7+67.0	265 ± 2	875 ± 3	10.3 ± 0.1	13.4 ± 0.1	17 733 ± 171	42.5 ± 0.3	5.1 ± 0.1	
PLCK_G200.6+46.1	350 ± 3	295 ± 2	5.7 ± 0.1	8.2 ± 0.1	9813 ± 172	37.5 ± 0.5	4.3 ± 0.1	22
PLCK_G231.3+72.2	350 ± 10	402 ± 5	7.5 ± 0.1	10.7 ± 0.1	12 913 ± 172	39.3 ± 0.4	4.7 ± 0.1	
PLCK_G244.8+54.9	300 ± 2	1135 ± 2	26.5 ± 0.2	36.3 ± 0.2	45 625 ± 344	50.0 ± 0.4	5.7 ± 0.1	9

Notes. The columns are: best-fit wavelength of the peak of the blackbody in the FIR; peak flux density at $\lambda_{\rm max}$ of the blackbody; FIR luminosity integrated from 8–1000 μm, including the magnification factor μ from our modified blackbody fit, and neglecting the possible presence of additional, hotter dust components; FIR luminosity derived from `DecompIR`, and including the fiducial mid-IR flux from star formation (see Sect. 7); star-formation rate, including magnification factor μ; dust temperature; dust mass, including the magnification factor μ; and AGN contribution to the FIR luminosity as obtained with `DecompIR`, where such a component was found.

the IRAM 30-m telescope, or else they represent sets of nearby, perhaps interacting galaxies. Alternatively, they may represent intrinsically complex gas kinematics in single star-forming environments, driven by the interplay of galaxy rotation, feedback, or perhaps turbulent motion within star-forming regions. High-resolution follow-up interferometry is currently being analysed to further elucidate their nature.

We fitted the emission lines shown in Fig. 3 with single Gaussian profiles to obtain the line FWHMs and integrated fluxes listed in Table 3. Integrated fluxes are $I_{\rm CO} = (7{-}34)\,{\rm Jy\,km\,s^{-1}}$, for $FWHM = 213{-}685\,{\rm km\,s^{-1}}$. A detailed analysis of the spectral properties of our sources that uses all our full sets of spectral line observations and that takes into account changes in line ratios in individual, kinematically distinct emission line regions into account will be presented elsewhere. Here we only use the spectroscopic redshifts, and the fluxes and FWHM line widths of the lowest-J CO transition observed in each source in order to demonstrate that these are indeed gravitationally lensed galaxies with extreme magnification factors.

In Table 3 we also compile luminosity estimates for the CO lines that we detect. We follow Solomon et al. (1997) in translating the integrated line fluxes into CO luminosities (in brightness temperature units), setting

$$L' = 3.25\times10^7\,I_{\rm CO}\left(\frac{\nu}{1+z}\right)^{-2} D_L^2(1+z)^{-3}. \quad (1)$$

Table 3. CO line properties obtained with EMIR on the IRAM 30-m telescope.

Source	Transition	Line flux $\mu\, I_{\rm CO}$ [Jy km s^{-1}]	Line luminosity $\mu\, L'$ [10^{11} K km s^{-1} pc^2]	$\mu\, M_{\rm mol}$ [$10^{11}\, M_\odot$]	*FWHM* [km s^{-1}]
PLCK_G045.1+61.1	4–3	22.9 ± 0.3	6.9 ± 0.1	5.6 ± 0.1	213 ± 11
PLCK_G080.2+49.8	3–2	9.2 ± 0.5	3.2 ± 0.2	2.6 ± 0.2	265 ± 12
PLCK_G092.5+42.9	4–3	34.3 ± 0.2	9.7 ± 0.1	7.8 ± 0.2	453 ± 3
PLCK_G102.1+53.6	3–2	5.7 ± 1.8	2.4 ± 0.7	2.0 ± 0.2	252 ± 10
PLCK_G113.7+61.0	3–2	16.5 ± 0.2	5.0 ± 0.1	4.0 ± 0.2	528 ± 5
PLCK_G138.6+62.0	3–2	22.0 ± 1.1	6.8 ± 0.3	5.4 ± 0.1	514 ± 40
PLCK_G145.2+50.9	3–2	21.9 ± 0.8	12.7 ± 0.6	10.2 ± 0.2	685 ± 17
PLCK_G165.7+67.0	3–2	25.4 ± 0.3	6.8 ± 0.1	5.4 ± 0.1	576 ± 4
PLCK_G200.6+46.1	3–2	11.2 ± 0.1	4.9 ± 0.1	3.8 ± 0.1	458 ± 9
PLCK_G231.3+72.2	3–2	9.4 ± 0.2	3.9 ± 0.1	3.0 ± 0.1	257 ± 8
PLCK_G244.8+54.9	3–2	7.4 ± 1.0	3.3 ± 0.4	2.6 ± 0.2	382 ± 10

Notes. The columns are source name; CO transition; integrated line flux; line luminosity $\mu\, L'$ (in brightness temperature units) derived using Eq. (1); molecular gas mass (see Sect. 9 for details); and full width at half maximum of the emission lines.

Here the measured frequency ν is given in GHz, z is the redshift, D_L is the luminosity distance, the CO luminosity L' is measured in K km s^{-1} pc^2, and the integrated CO line flux is in Jy km s^{-1}. In Sect. 9 we will also derive molecular gas mass estimates and compare with the dust masses obtained from our SED fitting.

5. Dust properties

To further characterize our sources, we fitted their FIR-to-millimetre photometry with modified blackbody distributions between 250 μm and 2000 μm, using the Python `curve_fit` routine from the scipy package[3]. The results are shown in Fig. 4. Most photometry points were observed with roughly similar beam sizes between 15″ and 30″, and we only see single, very bright components in each image, which makes us confident that uncertainties related to confusion and multiple sources within the same beam do not dominate our photometry. We do see the foreground lensing sources at short wavelengths, between the optical and NIR, including the blue channels of WISE. However, their relatively blue colours and locations suggest that they do not contribute significantly to the long-wavelength emission.

In the restframe of our targets, our data cover the peak of the SED and extend well into the Rayleigh-Jeans tail of the dust emission, which is a particularly clean probe of the thermal emission of the coldest dust component, dominating the overall mass budget. We followed, e.g., Blain et al. (2003) to allow for a frequency-dependent optical depth of the FIR emission, which we model in the standard way through a power law with emissivity index $\beta = 2.0$ and a critical wavelength of 100 μm, at which the dust opacity becomes unity. This specific choice of β is somewhat arbitrary, but at the signal-to-noise ratio and sparse frequency sampling of our SEDs, the precise value has a minor impact (for plausible values of β between 1.5 and 2.0) for our study. For example, we find typical offsets in dust temperature $\Delta T_{\rm d} \approx 2$ K between $\beta = 1.5$ and $\beta = 2.0$, comparable to our other uncertainties.

These fits correspond to dust temperatures of $T_{\rm d} = 33$–50 K, with no significant trend with redshift (Table 2). Uncertainties were derived from Monte Carlo simulations, where we varied the measured flux density in each band 1000 times within the measurement uncertainties, before fitting the SED in the same way as for the data.

The high infrared luminosities and dust temperatures of *Planck*'s Dusty GEMS suggest that most of the radiation in our sources comes from dense star-forming clouds, which is why we consider the optically thick case more relevant to our analysis. We note, however, that had we fit for optically thin emission, we would have derived temperatures between $T_{\rm d} = 30$ K and 41 K, lower by 3 K to 11 K in each individual source. Figure 4 shows that all sources are adequately fit with a single temperature component, in spite of a slight, systematic underestimate of the 850 μm, or alternatively, slight overestimate of the 500-μm flux density.

The temperature range we find does not differ significantly from those of other strongly lensed samples of high-redshift dusty star-forming galaxies selected in the FIR and (sub-)mm. This is illustrated in Fig. 5. It is interesting that the temperature range of our sources includes those of typical starburst galaxies at high redshift, as well as the lower temperatures of more gradually, but still intensely, star-forming galaxies along the main sequence (e.g., Elbaz et al. 2011). We do not find an obvious trend of dust temperature with redshift. This may either be due to the small number of targets observed over a relatively small redshift range, or because we are sampling environments with a range of properties within individual galaxies.

We derive infrared luminosities by integrating over our best-fit single-component modified blackbody SEDs between 8 μm and 1000 μm in the rest-frame, using the flux densities given in Table 1 and dust temperatures in Table 2. Luminosities thus obtained are in the range $L_{\rm FIR} = (4.6$–$26.5) \times 10^{13}\, \mu^{-1}\, L_\odot$, including the unknown gravitational magnification factor μ. Following Kennicutt (1998) we set $SFR[M_\odot\,{\rm yr}^{-1}] = 4.5 \times 10^{-37}\, L_{\rm FIR}$ [W], finding star-formation rates $SFR = 8000$–$46\,000\, \mu^{-1}\, M_\odot\,{\rm yr}^{-1}$, suggesting high intrinsic star-formation rates and high magnification factors. Corresponding apparent dust masses are $M_{\rm d} = (3.5$–$11) \times 10^9\, \mu^{-1}\, M_\odot$ (Table 2).

Figure 4 shows that we cover the peak of the dust SED for most sources, but nonetheless our sensitivity to warmer dust components probed in the FIR shortwards of 250 μm (60–80 μm in the rest-frame) is limited, and we are likely to miss emission from warmer dust components. Through template fitting with `DecompIR` (Mullaney et al. 2011), which we will further discuss in Sect. 7, we derived fiducial correction factors between the modified blackbody fits obtained here, and the templates

[3] http://docs.scipy.org/doc/scipy/reference/generated/scipy.optimize.curve_fit.html

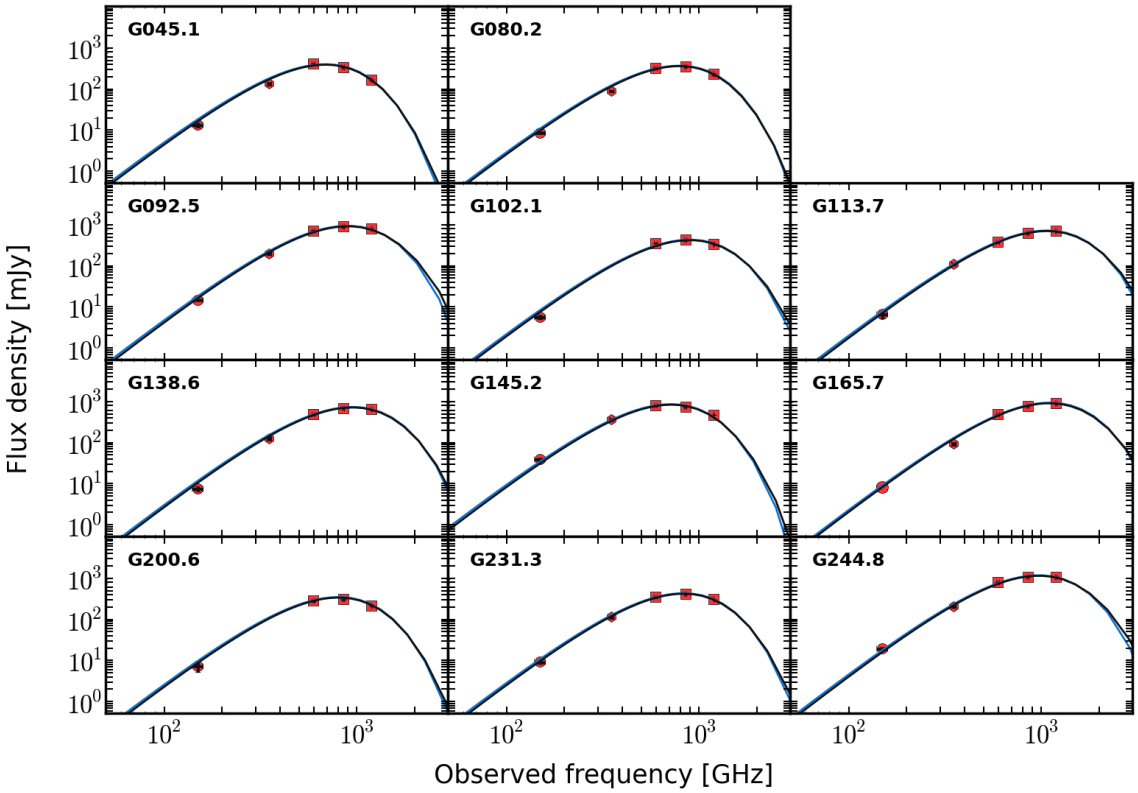

Fig. 4. Modified blackbody fits to the FIR-to-millimetre photometry of our sources as obtained with *Herschel-SPIRE* at 250, 350, and 500 μm, with JCMT/SCUBA-2 at 850 μm (for eight sources), and with IRAM/Gismo at 2 mm. The light and dark blue curves show the blackbody curves for optically thin and optically thick dust, respectively. Error bars are printed in black, and are smaller than the symbols showing the photometric data points.

we used to accommodate our FIR-to-submillimetre photometry (and constraints from WISE at 22 μm within the same SED fit). We thus find that our modified blackbody fits may underestimate the IR luminosity of our targets by 10–30%. We also list the respective values obtained from `DecompIR` in Table 2. Taken together, the direct estimate from the modified blackbody fits, and those from the templates, set a plausible range of luminosities. These luminosities would need to be corrected towards larger values if an additional warmer dust component was found with infrared constraints shortward of 250 μm.

We follow, e.g., Greve et al. (2012) in estimating dust masses, $M_{\rm d}$, by setting

$$M_{\rm d} = \mu^{-1} \frac{D_L^2 S_{\nu_0}}{(1+z)\kappa_{\nu_{\rm r}}} \left(B_{\nu_{\rm r}}(T_{\rm d}) - B_{\nu_{\rm r}}(T_{\rm CMB}(z))\right)^{-1} \quad (2)$$

where D_L is the luminosity distance to redshift z, S_{ν_0} the flux density at the observed frequency $\nu_{\rm r}(1+z)^{-1}$, which we set to 600 GHz (corresponding to the 500 μm band of `SPIRE`). $T_{\rm CMB}$ is the CMB temperature at redshift z. We used $\kappa_{\nu_{\rm r}} / \left(m^2\,{\rm kg}^{-1}\right) = 0.045 \times (\nu_{\rm r}/\ 250\ {\rm GHz})^{\beta}$, with $\beta = 2.0$ as already stated above. With this approach and these assumptions, we find dust masses of $M_{\rm d} = (3.5-11)\times10^9\ \mu^{-1}\ M_\odot$, with the unknown gravitational magnification factor μ. Results for individual sources are listed in Table 2.

6. Signatures of gravitational lensing

6.1. Flux densities and morphologies

The first observational hint that our targets might indeed be strongly gravitationally lensed galaxies is their sheer brightness and small angular size below 18″ (the FWHM of the SPIRE point spread function at the highest frequency, 250 μm), whereas 90% of the 234 Planck high-z candidates with *Herschel-SPIRE* follow-up consist of multiple sources. Unlensed high-redshift galaxies with FIR flux densities as high as those of our sources are very rare. For example, for flux densities $S_{350} > 400$ mJy at 350 μm and near the peak of the FIR SEDs of most GEMS, the Béthermin et al. (2012) models predict 3 sources sr^{-1} at $z \geq 2$ that are not, and 53 sources sr^{-1} that are gravitationally lensed. For a given source at these flux densities, it is therefore much more likely to find a gravitationally lensed galaxy than a galaxy in the field. We emphasize that this is true only for galaxies with confirmed high redshifts like the GEMS. The overall population of bright FIR galaxies is at much lower redshifts and has bluer FIR colours.

Given that more typical high-z galaxies in the field have FIR flux densities of few 10s mJy, the observed flux densities of our sources make us expect magnification factors of at least a few and perhaps greater than 10, even if these were intrinsically amongst the most luminous sources on the sky. For more moderate, more typical intrinsic flux densities, the gravitational magnification would be accordingly higher. The one alternative interpretation could be that these are multiple, highly concentrated galaxies within projected distances of a few tens of kpc, so that they are not resolved into individual galaxies by the SPIRE beam, which corresponds to about 120 kpc at $z \approx 2$ (for an example see Ivison et al. 2013).

More direct evidence that our sources indeed have a lensing nature comes from their morphologies. Strongly gravitationally lensed galaxies may either be single or multiple compact images seen near the intervening foreground lensing source, giant

arcs extending over several arcseconds, or even partial or complete Einstein rings. However, reaching the required spatial resolutions of about 1–2″ or better requires either deep optical or NIR imaging for sources that are not too heavily obscured, or, alternatively, sub-mm or millimetre interferometry.

Figure 1 shows the *Herschel* image as contours overlaid on optical imaging, and Fig. 2 the dust morphology obtained with the SMA at 850 μm. These figures clearly show that our sources are either single, compact objects at 2″ resolution (as is the case for, e.g., PLCK_G244.8+54.9 and PLCK_G138.6+62.0), or giant arcs (e.g., PLCK_G145.2+50.9 and PLCK_G080.2+49.8). PLCK_G244.8+54.9 and PLCK_G138.6+62.0 have flux densities of 1054 ± 10 and 664 ± 8 mJy, respectively, making it implausible that these are individual high-redshift galaxies if not benefitting from a strong boost from gravitational lensing through a massive foreground source. At a 2″ beam, intrinsic source sizes of unlensed galaxies would be at most 16 kpc, making it implausible to see a small group of high-redshift galaxies within a single beam.

Our sources are associated with overdensities of massive intervening galaxies at intermediate redshift, either galaxy groups or clusters. Table 1 lists the redshifts of the brightest intervening galaxies along the line of sight to our targets, which were taken from the SDSS. They are either photometric redshifts or (in a few individual cases highlighted in Table 1), spectroscopic redshifts. A detailed analysis of the lensing structure based on our own proprietary optical/NIR photometry obtained at the CFHT and the VLT is on-going. The only target associated with a foreground object for which we currently have no good redshift estimate is G145.2+50.9, which forms a near-complete Einstein ring with a diameter of 10″ around a very red foreground source, which we currently only detect in the J-band. For this galaxy, our optical/NIR photometry is not yet complete, and we must therefore defer a detailed analysis of the foreground source to a later publication.

In the rest of this section we will present additional empirical evidence to illustrate that all of our sample consists of strongly gravitationally lensed galaxies, including those for which we do not yet have morphological constraints.

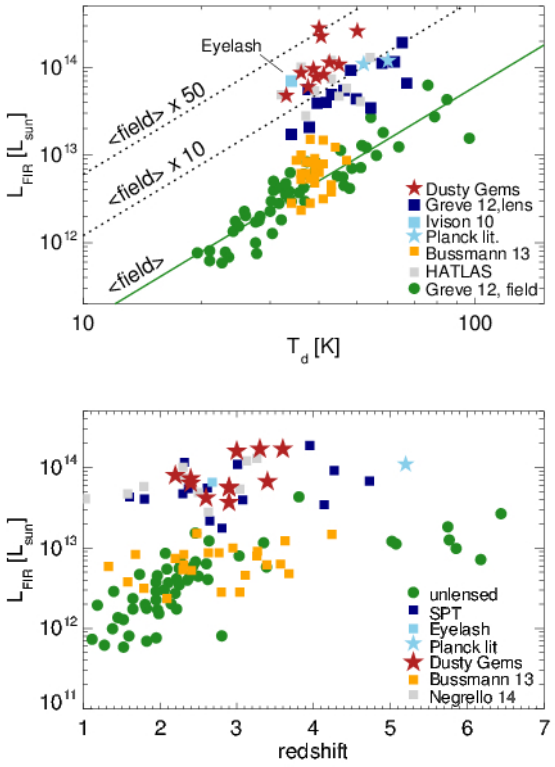

Fig. 5. Characterizing our sources by their FIR luminosities, dust temperatures, and redshifts. *Top*: FIR luminosities versus dust temperatures. The Dusty GEMS targets are shown as red stars on top of the comparison samples of strongly lensed sources taken from the literature (see Greve et al. 2012, and references therein), lens candidates from the SPT survey (Vieira et al. 2013), the Eyelash (Ivison et al. 2010b), and the two *Planck* lenses that were discovered prior to our work (Combes et al. 2012; Fu et al. 2012). The solid line shows a fit to the general population, while the dotted lines show magnification factors of 10 and 50. *Bottom*: FIR luminosity as a function of redshift. In the lower panel, our sources fall near the most luminous gravitationally lensed galaxies at similar redshifts; however, these are strongly dominated by AGN, like APM 08279+5255, whereas our sources are bona fide starbursts, at least in the image plane. This explains the greater luminosities at lower dust temperatures seen in the top panel.

6.2. FIR dust continuum

Greve et al. (2012) suggested the use of the relationship between T_d and L_{FIR} as an empirical indicator of whether a source is strongly gravitationally lensed. According to the Stefan-Boltzmann law, the luminosity emitted by a modified blackbody at a given temperature depends only on the size of the emitting surface and the emissivity. Therefore, if our galaxies form a subset of the generic population of dusty, intensely star-forming high-redshift galaxies, the gravitational magnification factor should lead to an apparent increase in dust luminosity at a given temperature for gravitationally lensed galaxies, compared to unlensed galaxies.

In Fig. 5 we show where our sources fall on a plot of dust temperature versus FIR luminosity, compared to the galaxies of Greve et al. (2012) and other sources from the literature. It is immediately clear that our sources are significantly brighter at a given temperature than galaxies in the field, and even brighter than most of the previously known gravitationally lensed galaxies. The dashed lines illustrate luminosities that are 10 times and 50 times brighter than expected from a simple least square fit to the population of field galaxies (green solid line). We highlight the Cosmic Eyelash of Swinbank et al. (2010) and the two previously confirmed gravitationally lensed galaxies with *Planck* counterparts (Fu et al. 2012; Combes et al. 2012).

For a more explicit, although not necessarily very precise estimate that exploits this relationship between dust temperature, luminosity, and source size, we can use the Stefan-Boltzmann law directly to infer the magnification factor from the observed luminosity and dust temperature. The approach is described in detail in Greve et al. (2012). Given the somewhat higher dust temperatures of our lens candidates compared to the SPT sources of Greve et al. (2012), we have a larger range of "effective" Stefan-Boltzmann constants (which correct for the lower emissivity of a modified relative to a genuine blackbody), σ_{eff}/σ = 0.5–0.65, and apparent emitting surfaces that are between 8 and 40 times larger than those of typical FIR galaxies, implying magnification factors that are roughly similar. These results are also shown in Fig. 6. We note that the estimates are very uncertain, since they assume that each high-redshift galaxy has a similar emissivity, that the dust becomes optically thick at similar wavelengths, and that the interstellar medium (ISM) of the galaxies is dominated by a uniform dust component with a single temperature. Each of these assumptions can

only be approximately true, and this will lead to uncertainties of at least factors of a few in this estimate. This is illustrated by the magnification factor of about 10 of the "Cosmic Eyelash," which we constrained with the same approach, and which falls into a very similar region of the diagram as our sources. The "Cosmic Eyelash" has intrinsic magnification factors of 20−60 (Swinbank et al. 2011), with an average factor of 32.5. In spite of these caveats, Fig. 5 provides additional indirect support that our sources are indeed strongly gravitationally lensed galaxies.

6.3. Molecular gas lines

More empirical evidence for strong gravitational magnification of our galaxies comes from the emission-line properties that we measured with EMIR on the IRAM 30-m telescope. To demonstrate that their galaxies discovered through the H-ATLAS survey are indeed strongly gravitationally lensed, Harris et al. (2012) compared the CO(1–0) line luminosities L' and FWHMs of their galaxies with the sources of Bothwell et al. (2013), who had found a broad trend between luminosity and line width in galaxies in the field (Fig. 6). The galaxies of Harris et al. (2012) and other strongly gravitationally lensed galaxies from the literature stand out by 1–2 orders of magnitude above this relationship, owing to the boost in line luminosity by the gravitational lens. In contrast, lines are expected to be as broad as in field galaxies (or narrower, because smaller regions of the large-scale velocity field of the galaxy are being observed). If a small region in a galaxy is magnified by strong gravitational lensing, then only parts of the rotation curve will be sampled, and turbulent motion will also be smaller. Therefore, observed line widths should be narrower than if galaxy-wide radii are probed, as in field galaxies.

Figure 6, inspired by Fig. 7 of Harris et al. (2012), shows where our sources fall relative to the Harris et al. sample and those in the literature. Our sources span a large range in FWHM in this diagram, but are all clearly within the regime of gravitationally lensed galaxies. The FWHMs of some of our targets may be as large as those of overdensities of multiple lensed sources that are at best moderately gravitationally lensed like the example in Ivison et al. (2013). Their luminosities are factors of a few brighter, placing them firmly above the field galaxies, and into the lens regime. The example of the Cosmic Eyelash, which has a magnification factor of 20–60 shows however that the lensing factor derived from the position of a source in this diagram can only be an approximate indicator. The line luminosities and profiles provide additional evidence in support for the lensing hypothesis.

7. Dust heating and AGN content

Many dusty high-z starburst galaxies host powerful AGN. For example Alexander et al. (2005) find that 75% of submillimetre galaxies have AGN detected at X-ray wavelengths (but see also Laird et al. 2010, who find significantly lower fractions of 10–20%). Powerful, obscured AGN could contribute significantly to $L_{\rm FIR}$, which would lower the magnification factors that are needed to explain the extraordinary apparent brightness of our targets. The inferred dust temperatures of our sources are akin to those of other high-z starburst galaxies and would be very low compared to those of obscured quasars, which are typically above 70 K, often far above. However, our estimates may be biased towards low temperatures because of the absence of mid-IR constraints shortward of 50–80 μm in our data sets. This

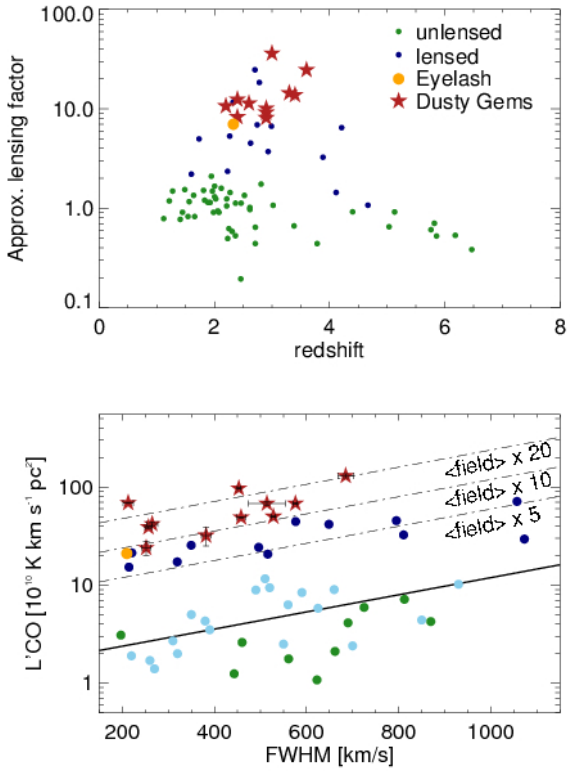

Fig. 6. *Top*: order-of-magnitude estimate of the gravitational magnification factor derived from the dust temperature and FIR luminosity of our sources compared to FIR and sub-mm galaxies in the field (see Sect. 6.2 for details). *Bottom*: CO emission-line luminosity as a function of FWHM line width, using the same symbols as in the top panel, with additional light blue dots showing those sources of Bothwell et al. (2013), which are neither gravitationally lensed nor AGN hosts. The solid and dashed lines show the best linear fit to the sample of field galaxies, as well as shifts of this line corresponding to magnification factors of 5, 10, and 20. Error bars show the 1σ uncertainties of our single-component Gaussian line fits.

makes it worthwhile to investigate in more depth what the possible AGN contribution might be to the infrared luminosity budget of our targets.

Not all AGN play a significant role for the total infrared luminosity budget of their host galaxies. Ideally, searching for obscured AGN activity in our targets would require PACS or at least deep *Spitzer* 24-μm photometry, to sample the dust SED shortward of about 100 μm in the rest-frame. Since our sample was only discovered with SPIRE in the last weeks of the *Herschel* mission, such data sets are not available. Additionally, in spite of their exceptional brightness (for high-redshift targets), they are still too faint to obtain robust mid-IR photometric constraints with SOFIA. We might therefore not be able to give tight constraints on the presence of weak AGN activity in all of our sources, however, most important for our purposes here is to show that AGN radiation is not energetically dominant in our sources (i.e., they do not contribute >0.5 $L_{\rm bol}$), which would have important implications for the estimated star formation rates, plausible ranges of intrinsic infrared luminosities, and gas excitation.

7.1. WISE 22 μm photometry

WISE in the 22-μm band covers rest-frame wavelengths between 4 and 7 μm for our sources, i.e., the far blue tail of hot dust

emission from powerful AGN. Consequently, WISE has been successfully used to identify heavily obscured AGN at high-z (e.g., Yan et al. 2013). All of our sources are bright enough to be detected in WISE imaging at 22 μm, and seven are included in the WISE catalogues. The remaining four can be seen as very faint sources in the WISE images, but are not bright enough to obtain robust flux measurements. We will in the following use the flux measurements from the WISE catalogs and treat the 5σ rms of this catalog at 5.4 mJy as upper limit for the fainter sources. Individual flux densities are listed for all sources in Table 1.

Although we do detect nearby bluer sources in each case at 3.4 μm, 4.6 μm, and 12 μm, the SED in all but one source falls off too steeply in the three blue WISE bands to contribute significantly to the 22 μm detections. Their colours suggest that these are low-to-intermediate-redshift objects, which we consider part of the intervening lensing structure.

7.2. Constraining AGN dust heating with DecompIR

We used the publicly available package DecompIR (Mullaney et al. 2011) to constrain the potential contribution from AGN emission to the infrared SED, using our six available data points between 22 μm and 2 mm, as listed in Table 1. DecompIR performs χ^2 fits to infrared SEDs using composites of empirically constructed templates of starburst galaxies and AGN. We only have six photometric data points, but we sample the Rayleigh-Jeans tail and the peak of the SED of the emission from the coldest dust component, and therefore constrain the most abundant dust component well. We have spectroscopic redshifts and hence can estimate robust dust temperatures, and therefore we consider this part of the SED to be well constrained. Our main uncertainties are blueward of the dust peak, which we only sample with the 22 μm data point from WISE and the 250 μm data point from SPIRE. The 250 μm band corresponds to 50–80 μm in the rest-frame for our targets, is slightly blueward of the peak of the dust emission in most of our sources (Fig. 4), and falls near the expected peak of the infrared emission from hot dust in the AGN torus in most templates (e.g., Polletta et al. 2007; Nenkova et al. 2008). The SEDs of powerful AGN host galaxies at high redshifts are typically dominated by AGN emission at these wavelengths (e.g., Sajina et al. 2012; Drouart et al. 2014).

The DecompIR software package provides a small set of SED templates, derived from nearby starburst galaxies. One complication in using these templates for our sources is that we find a range of dust temperatures, which are not all well represented by existing templates. This would lead to considerable (but somewhat artificial) discrepancies in the template fitting that would be hard to overcome without a self-consistent model of the mid-to-far-IR SED of high-redshift galaxies, which does not yet exist. To avoid such mismatches, while make optimal use of our existing constraints without overinterpreting the mid-IR data, we therefore constructed a simple starburst template for each of our galaxies from the "SB2" template of DecompIR (corresponding to the SED of NGC 7252, Mullaney et al. 2011), but correcting for the mismatch in dust temperatures. We therefore fitted and removed from the template the modified blackbody contribution from cold dust in the FIR. The residual is a template of the SED in the mid-IR only, to which we added the modified blackbody emission obtained from our FIR fits, using the measured temperature for each source. We selected this particular template, because it provided the best match to the FIR and submillimetre measurements of the dust peak and Rayleigh-Jeans tail, with no regard of the goodness of fit of the 22 μm observations. For the AGN component, we simply used the Polletta et al. (2007) type-2 QSO template which is already part of DecompIR.

Figure 7 shows that we can rule out a bolometrically dominant AGN contribution from buried quasars, in all cases. Only three galaxies have best-fit results formally inconsistent with pure starbursts. In PLCK_G092.5+42.9 and PLCK_G244.8+54.9, the putative AGN contribution to the FIR luminosity is below 10%, and it is below 30% in PLCK_G145.2+50.9. In all other cases, DecompIR finds the best fit for a pure starburst SED.

Figure 7 also shows the 90% completeness limits of the IRAS faint source survey (Moshir et al. 1992), 120 mJy and 440 mJy at 60 μm and 100 μm, respectively (green downward arrows). Although these limits are not constraining for the SED fits that we obtained with SPIRE, SCUBA-2, GISMO, and WISE (and were therefore not included in our DecompIR fits) they do illustrate that a hypothetical bright quasar component would have led to a 60 μm detection at least in our brightest targets. In Fig. 8 we illustrate the impact of fiducial AGN contribution of 0.1, 0.3, and 0.5 $\times$ $L_{\rm FIR}$ on the example of G138.6+62.0, a source with rather average FIR brightness and 250-to-350 μm colour in our sample.

Obviously, these fits are uncertain, given that they cover the far blue wing of the dust SED expected from bright AGN, and a spectral range that has important contributions from rich mid-IR spectral features, in particular from Polycyclic Aromatic Hydrocarbons (PAH), which dominate the infrared SEDs of starburst galaxies between about 3 μm and 10 μm (e.g., Armus et al. 2007).

The equivalent widths of the PAH bands have a wide dispersion in high-redshift galaxies (e.g., Fiolet et al. 2010), and are generally larger than those measured in low-redshift ULIRGs, including NGC 7252, which we used as template in our DecompIR fits. Additional uncertainties come from the stellar continuum, which reaches comparable strength to the dust continuum in the wavelength range covered by the 22 μm observations, about 5–7 μm, and whose shape depends strongly on the specific star-formation rate, star-formation history, and geometry of dust obscuration in the host galaxy. Compared to the average mid-IR SED of starburst galaxies (Brandl et al. 2006), the stellar continuum in NGC 7252 seems relatively faint, and Sajina et al. (2012) also found that the mid-IR continuum of high-redshift starburst galaxies seems to be brighter than in low-redshift galaxies. Other spectral features might also contribute to boosting the observed 22 μm flux density. For example Fiolet et al. (2010) report the detection of warm H_2 line emission at 6.9 μm in the rest-frame. Moreover, the foreground galaxies may also contribute to the 22 μm flux, given the 12″ beam of WISE. However, all these uncertainties would only act to lower the putative intrinsic contribution of AGN heating relative to what we observe. It will of course be very interesting to study the mid-IR spectral properties of our sources in depth once that JWST/MIRI will become available.

Relying upon these arguments, we conclude that the dust heating in our sources is not dominated by heavily obscured quasars, but that the *Planck* Dusty GEMS are genuine starburst galaxies with at most a minor contribution of AGN heating to the dust emission and the bolometric energy budget of our sources. Of course this only refers to the regions that we are seeing under the gravitational microscope of the foreground lensing systems. The global energy budgets of AGN and star formation in these

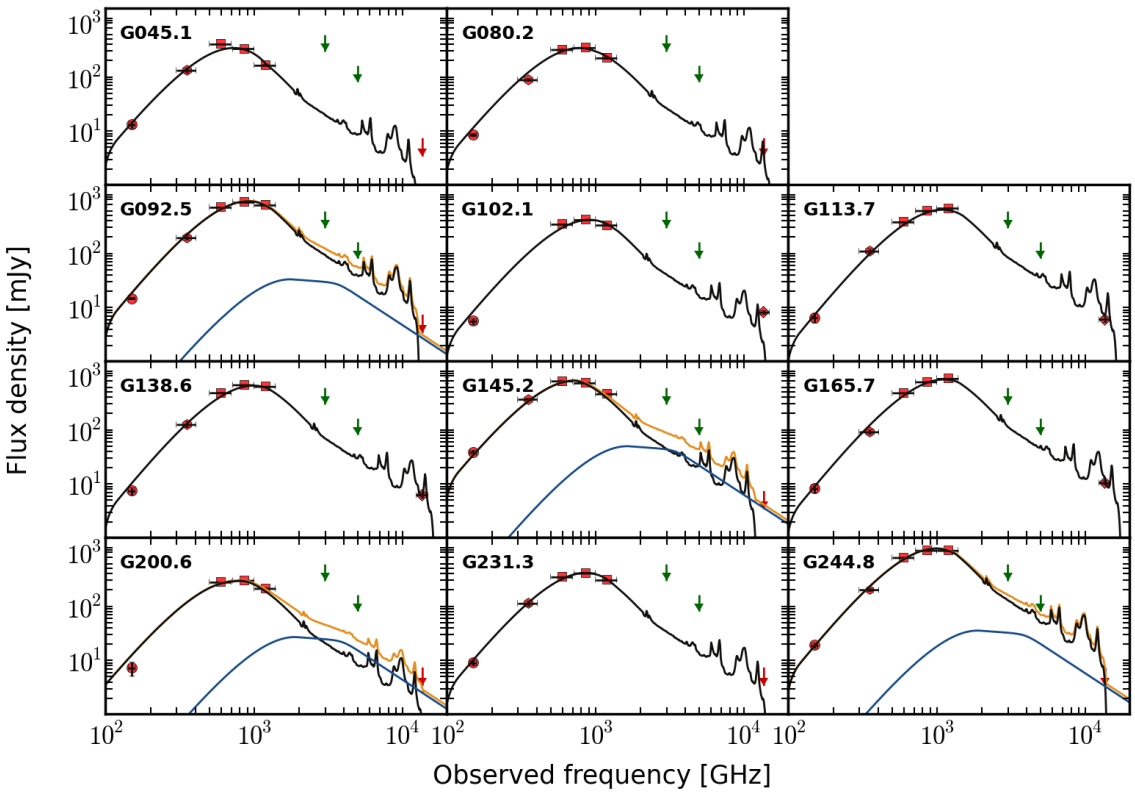

Fig. 7. Infrared-to-millimetre SEDs of all of our 11 sources obtained using `DecompIR` (Mullaney et al. 2011). Red dots show our data points, where the error bars along the abscissa indicate the width of each band. The error bars along the ordinate are often smaller than the symbol size. Green downward arrows show the 90% completeness limit of the IRAS all-sky survey at 60 and 100 μm, respectively. Red downward arrows at 22 μm show the 5σ upper limits provided by the WISE catalogs, where the counterparts were fainter than the 5.4 mJy flux limit of the WISE catalog. Black, blue, and yellow lines show the starburst and AGN component (if an AGN was fitted), and the sum of both, respectively.

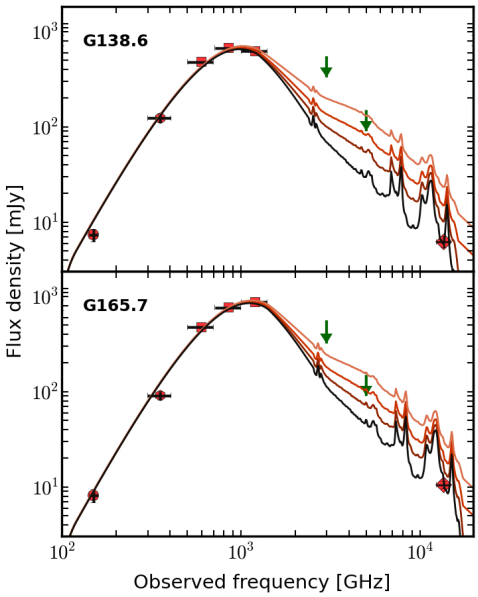

Fig. 8. A schematic illustrating the impact of 0.1, 0.3, and 0.5 × $L_{\rm FIR}$ of AGN contamination to the shape of the SED of our sources, on the example of G138.6+62.0 and G165.7+67.0.

galaxies may be different, if the AGN lies along a line of sight that is not strongly magnified (see also Serjeant 2012).

8. FIR-radio correlation

Given the extraordinary brightness of our targets on the sky, we can use the 1.4 GHz VLA survey of the northern sky, FIRST (Becker et al. 1995), to search for counterparts of our sources at an observed frequency of 1.4 GHz (between 4.5 and 6.4 GHz in the rest-frame). We find that six of our sources have counterparts within 5″ of a source in the FIRST catalogue, and the other five have sensitive upper limits (see Table 4). Here 5″ corresponds to the beam size of FIRST. We assume a radio spectral index $\alpha_{1.4} = -0.8$ (as is appropriate for star-forming regions, Condon 1992) to convert these flux densities to a monochromatic radio flux density at rest-frame 1.4 GHz, as well as to estimate a radio power. For galaxies without detections we use the 3 σ upper limits implied by the rms given in the FIRST catalogue. Results for individual sources are listed in Table 4. All sources are listed in the FIRST catalog as marginally resolved, with deconvolved sizes between 1.5″ and 7″. The 5″ beam of FIRST is not always sufficiently small to rule out contamination from a radio nucleus in the foreground lensing galaxy. However, most sources are isolated enough to conclude that the radio counterpart is at the position of the high-redshift galaxy, and not coincident with a massive, intermediate-redshift galaxy that could host a radio-loud AGN. This is particularly the case for PLCK_G244.8+54.9.

The FIR radio correlation is commonly parametrized as $q = \log L_{\rm IR}/(3.75 \times 10^{12}\,{\rm W}) - \log L_{1.4}/({\rm W\,Hz^{-1}})$, where $L_{\rm IR}$ is measured in the range 8–1000 μm in the rest-frame, and the centimetre continuum at a rest-frame frequency of 1.4 GHz. Early *Herschel* results suggest $\langle q \rangle = 2.4 \pm 0.12$ in the local Universe (Jarvis et al. 2010), although values can change

Table 4. Radio continuum properties extracted from the FIRST catalogue.

Source	Dist.	$\mu_{1.4}\, S^{\rm int}_{1.4}$	$\mu_{1.4}\, L_{1.4}$	q
	[arcsec]	[mJy]	[10^{25} W Hz^{-1}]	
PLCK_G045.1+61.1		<0.135	<3.2	>2.4
PLCK_G080.2+49.8		<0.135	<1.8	>2.4
PLCK_G092.5+42.9	0.9	1.50 ± 0.16	11.2	2.35 ± 0.11
PLCK_G102.1+53.6		<0.149	<2.5	>2.5
PLCK_G113.7+61.0	3.0	1.9 ± 0.14	6.9	2.2 ± 0.08
PLCK_G138.6+62.0	2.7	2.01 ± 0.16	7.3	2.1 ± 0.08
PLCK_G145.2+50.9		<0.144	<3.9	>2.8
PLCK_G165.7+67.0	4.1	3.41 ± 0.15	10.1	2.0 ± 0.04
PLCK_G200.6+46.1	1.1	1.23 ± 0.14	6.9	1.9 ± 0.11
PLCK_G231.3+72.2		<0.151	<2.5	>2.5
PLCK_G244.8+54.9	3.2	2.26 ± 0.14	13.6	2.3 ± 0.06

Notes. The columns are: source name; relative distance between the SPIRE position at 250 μm and the position of the FIRST counterpart, if detected within 5″; integrated flux density at 1.4 GHz from the FIRST catalogue and gravitational magnification factor of the radio component, $\mu_{1.4}$; radio luminosity at 1.4 GHz in the rest-frame and gravitational magnification factor of that component, $\mu_{1.4}$, for sources without 1.4 GHz detections, the luminosities are derived from 3× the rms given in column 3; the Ratio between radio and FIR luminosity (see Sect. 8), i.e. the q-parameter.

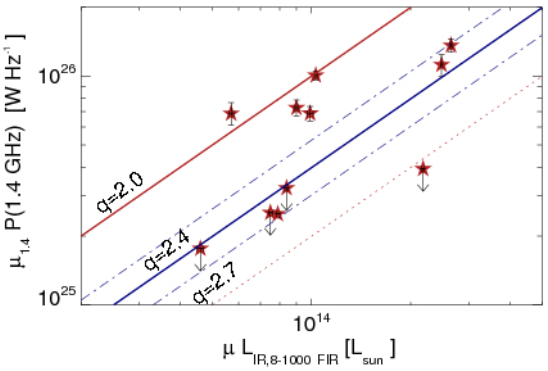

Fig. 9. Far-infrared radio correlation of our sources, as discussed in Sect. 8. $\mu_{\rm FIR}$ and $\mu_{1.4}$ correspond to the magnification factors appropriate for the dusty and 1.4 GHz synchrotron emission, respectively. Solid blue and red lines show the relationship for $q = 2.4$ and 2.0, respectively, while the red dotted line is for $q = 2.7$. The dot-dashed lines show the $\pm 1\sigma$ scatter about $q = 2.4$ at low redshift from Jarvis et al. (2010).

considerably even within individual galaxies (e.g., Tabatabaei et al. 2013). Towards higher redshifts, results show less of a consensus. Kovács et al. (2006), Vlahakis et al. (2007), Michałowski et al. (2010), and Bourne et al. (2011) report an increase in radio power at a given FIR luminosity at $z \gtrsim 1$, with $\langle q \rangle = 2.0$. However, several studies (e.g., Ivison et al. 2010a,b; Sargent et al. 2010; Thomson et al. 2014) find average values in the range $q = 2.4$–2.7, out to $z \approx 2$. Most of these studies use stacking analyses to overcome the inherent faintness of high-redshift galaxies in the FIR and sub-mm and in the radio, and are based on ground-based data that do not sample the FIR dust SED very well. In the Cosmic Eyelash, a single, strongly lensed galaxy at $z = 2.4$ with *Herschel-SPIRE* coverage, Ivison et al. (2010b) find $q = 2.4$.

In Fig. 9 we show where our sources fall relative to the local FIR-radio correlation, assuming that differential lensing between the FIR and radio synchrotron emission does not play a major role in our case. Four of our sources are brighter by up to about 0.4 dex in the radio, and fall outside the 1σ scatter around the distribution of q parameters of low-redshift galaxies. Six galaxies fall within 1σ from this relationship, however, three of these galaxies only have upper limits on q, and would fall outside the 1σ scatter if we had adopted 1σ, instead of 3σ upper limits. One galaxy has $q > 2.7$ at 3σ.

If the 1.4 GHz emission is caused by star formation, then the lower q values cannot be caused by our assumption of the spectral index $\alpha_{1.4} = -0.8$. Only for flat radio SEDs ($\alpha_{1.4} = -0.2$ or above, which would only be possible for an AGN) would our highest-q sources be consistent with the FIR-correlation and $q = 2.4$. If this were the case, our sources with the highest q parameters (i.e., the brightest sources in the FIR relative to the radio) would fall well above $q = 3$.

One way of obtaining lower q-values, as has been pointed out several times before (e.g., Vlahakis et al. 2007; Bourne et al. 2011) is through radio emission from a central AGN. This has an interesting theoretical aspect, since it has been proposed (e.g., Silk & Norman 2009) that gas compression caused by expanding radio sources in massive high-z galaxies may in fact contribute to boosting the star-formation efficiency in intense high-z starbursts. However, although contamination with nuclear radio emission may be a particular concern for stacking analyses (where one or a few relatively bright radio sources may affect the average result of the overall sample), in our case this explanation seems to be less likely. First, the radio sources are spatially resolved in FIRST, suggesting they are extended, just like the star formation. Even if the Dusty GEMS have extended radio sources, the gravitational lensing would need to amplify the radio emission by similar amounts to that of the star formation in most of our sources; this appears relatively unlikely, given that the AGN radio morphologies of high-z galaxies are very different from those of the dust and stellar components (e.g. Sajina et al. 2007).

As a second counter argument, our SED fits have already disfavoured the presence of very luminous AGN. Although galaxies are known to host central radio sources without bright bolometric emission, the host galaxies of such AGN tend to have little dust, gas, and on-going star formation. And although relatively faint AGN may be present without leaving strong signatures in the dust SEDs, only a subset of those should be radio loud. Even optimistic results (e.g., from Sajina et al. 2007), imply that only up to about 30% of dusty high-z starburst galaxies may host moderately bright ($P_{1.4} \approx 10^{25}$ W Hz^{-1}, comparable to our sources for magnification factors of order 10) nuclear radio sources that are as bright as or brighter than the star formation itself. In addition, these sources are classified as AGN in the mid-IR. We note that we have not found any obvious trends between the q-parameter and possible probes of AGN contamination like dust temperature or $L_{\rm FIR}$. We also do not find a correlation between the flux density at 22 μm and the 1.4 GHz radio emission.

As an alternative, the offsets towards larger and smaller q-parameters may be caused by the star-forming environments themselves. Lacki & Thompson (2010) suggest that enhanced synchrotron emission from cosmic rays in star-forming galaxies at high redshift could be one outcome of the strong turbulence observed in these galaxies (e.g., Förster Schreiber et al. 2009; Lehnert et al. 2009; Swinbank et al. 2011), which enhances the scale height of the gas, and lowers their volume density. In this

case, energy loss of cosmic rays through synchrotron radiation, bremsstrahlung, and other processes could be either enhanced or diminished, depending on the local magnetic fields and density distribution of the ISM; this could either decrease or increase the energy losses of the cosmic rays, making our sources either brighter or fainter (e.g., Murphy 2009). Other possible explanations, which might also involve the sources with unusually high q-parameters, include evolution in the dust properties, the age of the starburst (the radio should not probe starbursts with ages of less than a few times 10^7 yr or greater than a few times 10^8 yr, because of the timing of core-collapse supernovae, Bressan et al. 2002), and a top-heavy initial mass function (e.g., Baugh et al. 2005). It will be interesting to obtain high-resolution centimetre-wave maps of these sources, along with our gas and dust interferometry, to constrain the potential impact of differential lensing and to further elucidate how the q-parameter depends locally on the ISM properties in our sources.

9. Gas masses and gas-to-dust ratios

To determine the molecular gas mass (which is dominated by H_2) from the CO luminosity, we have to assume an empirical conversion factor, which is notoriously difficult to justify from first principles, and which is therefore still heavily debated in the literature, in particular for high-redshift galaxies (e.g., Daddi et al. 2010; Genzel et al. 2010; Glover & Mac Low 2011; Narayanan et al. 2012). The canonical value adopted for most high-z galaxies is $\alpha \approx 0.8\,M_\odot/(\mathrm{K\,km\,s^{-1}\,pc^2})$. This value was first derived by Downes & Solomon (1998) for the dense, circumnuclear, optically thick molecular gas discs in nearby ULIRGs, and is commonly adopted also for dusty starburst galaxies in the early Universe.

However, several studies in recent years (starting with Daddi et al. 2010 and Genzel et al. 2010) have called into question whether a single CO(1–0)-to-H_2 conversion factor may be appropriate to use for all high-z galaxies. Several attempts have therefore been undertaken to constrain α_{CO} either from dynamical mass estimates, or on theoretical grounds. One empirical approach suited for galaxies with well constrained dust mass measurements like ours, is to assume that high-z galaxies fall onto a similar relationship between gas-to-dust mass ratios and metallicities as found for SINGs galaxies in the local Universe (Leroy et al. 2008). Magdis et al. (2011) used this approach to confirm their α_{CO} determinations, which they previously obtained from dynamical mass estimates.

We can use our measurements of the dust mass, M_{d} (Sect. 6.2 and Table 2), and the CO line luminosity, L' (Sect. 4.3 and Table 3), to estimate ratios of L'/M_{d}, which scale with gas-phase metallicity (Leroy et al. 2008; Magdis et al. 2011). Using Fig. 3 of Magdis et al. (2011), we find that our measured range $L'/M_{\mathrm{d}} = 40$–140 corresponds to gas-phase metallicities $12 + \log(\mathrm{O/H}) \sim 8.9$–$9.3$. These values are appropriate for $\beta = 2.0$ (Sect. 6.2). Furthermore, we adopted a ratio $r_{32/10} = 1$ to convert from the luminosities of the observed mid-J CO lines to CO(1–0). This factor is expected for optically thick gas (e.g., Solomon & Vanden Bout 2005). In the Cosmic Eyelash, Danielson et al. (2011) measured $r_{32/10} = 0.7$.

High gas-phase metallicities correspond to small values of α_{CO} of ≤ 1.0. For example, if we use the linear fit between α_{CO} and metallicity of Genzel et al. (2012), we find conversion factors of about 0.4 at face value, although with large uncertainties. Likewise, Fig. 3 of Magdis et al. (2011) suggests $\alpha_{\mathrm{CO}} < 1.0\,M_\odot/(\mathrm{K\,km\,s^{-1}\,pc^2})$ for galaxies with L'/M_{d} ratios and metallicities as high as in our sources. This suggests that using the ULIRG conversion factor of $\alpha_{\mathrm{CO}} = 0.8\,M_\odot/(\mathrm{K\,km\,s^{-1}\,pc^2})$ is more appropriate than much higher factors of 3–5 $M_\odot/(\mathrm{K\,km\,s^{-1}\,pc^2})$, as previously adopted for more moderately star forming, disk-like high-redshift galaxies and the Milky Way. We stress that these results are measured in small regions of high-z galaxies, and are not necessarily representative of the average values in these galaxies (Serjeant 2012).

When using a common conversion factor $\alpha_{\mathrm{CO}} \approx 0.8\,M_\odot/(\mathrm{K\,km\,s^{-1}\,pc^2})$, we find molecular gas masses of 2–$10\times10^{11}\,\mu^{-1}\,M_\odot$ for *Planck*'s Dusty GEMS (including the gravitational magnification factor μ). Results for individual galaxies are listed in Table 3.

10. Integrated star-formation law

The tight correlation between molecular gas mass surface density and star-formation intensity over scales of around 100 pc to entire galaxies highlights how star formation depends on the available molecular gas reservoirs (i.e., the Schmidt-Kennicutt law, Schmidt 1959; Kennicutt 1998), although there is no consensus about a unique physical mechanism putting this relationship in place.

However, starting with, e.g., Daddi et al. (2010) and Genzel et al. (2010), several studies have emphasized in recent years that not all high-redshift galaxies may strictly obey the same empirical star-formation law, but that at a given gas surface density, starburst galaxies may be more efficient in turning their gas into stars. The reasons for this are still unclear, with possibilities ranging from changes in the stellar initial mass function (Baugh et al. 2005) to different star-formation efficiencies. For example, there may be more star-forming clouds in their ISM than in more quiescent high-z galaxies (Lehnert et al. 2013), or the star-formation efficiency per free-fall time could be higher (Dekel et al. 2009). What we can confidently assert (given the absence of dust with $T \gg 50$ K, faint 22-μm flux density, or excess radio emission) is that AGN do not play a dominant role in boosting the FIR continuum in the strongly amplified regions that we are seeing in our galaxies (Sect. 7). Given the close astrophysical connection between dust and gas in star-forming regions, we see no reason to believe that differential lensing plays an important role for our analysis of the gas conditions in the regions, which are amplified by the gravitational lenses. Of course, we must keep in mind that the gas and dust measurements obtained in small, selectively amplified regions of these galaxies are not necessarily representative of the average gas and dust properties in these galaxies on global scales (Serjeant 2012).

The relationship of FIR luminosity with CO line luminosity is a simple, empirical, and robust way of investigating this "star-formation law". It is directly related to the integral form of the Schmidt-Kennicutt law, because the FIR luminosity probing the emission from warm dust is an excellent tracer of star formation. CO line emission is mainly excited through collisions with H_2 and is the most commonly adopted proxy of the total molecular gas mass (e.g., Omont 2007).

In order to investigate whether our sources are representative of star formation in high-z starburst galaxies or more ordinary, but nonetheless very intensely star-forming galaxies on the "main sequence" (e.g., Elbaz et al. 2011), we use the molecular gas masses estimated from the CO luminosities (M_{H2}) and FIR luminosities (L_{FIR}), shown in Fig. 10, and compare with the correlations found by Daddi et al. (2010) and Genzel et al. (2010) for starburst galaxies, together with the more gradually, but nonetheless intensely star-forming high-z galaxies on

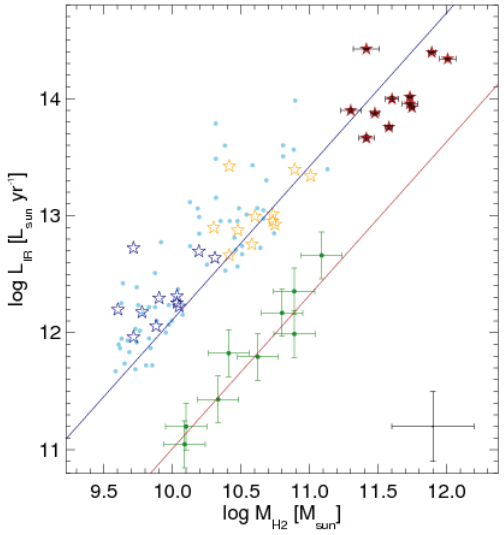

Fig. 10. Infrared luminosities ($L_{\rm IR}$) as a function of molecular gas mass for our sources. Red, yellow, and purple stars indicate the measured values (uncorrected for gravitational amplification), and the same values corrected by fiducial lensing factors of 10 and 50, respectively. In agreement with the dust-to-gas ratios discussed in Sect. 9 we adopt the classical "ULIRG" conversion factor $\alpha_{\rm CO} = 0.8\,M_{\odot}/({\rm K\,km\,s^{-1}\,pc^2})$ for all sources. The blue and red line indicate the relationships for starbursts and "main-sequence" galaxies emphasized by Daddi et al. (2010). Small dots show the low- and high-z samples of Daddi et al. (2010) for comparison. Light blue dots along the upper line show low- and high-z ULIRGs and SMGs, respectively. The filled dark green dots (with error bars) are BzK galaxies at $z \sim 2$; for details of these samples see Daddi et al. (2010). All error bars include the measurement uncertainties. The black cross in the lower right corner of the plot shows a fiducial factor 2 in statistical uncertainty.

the "main sequence". For this comparison, we use the integrated star-formation rates and molecular gas masses, adopting $\alpha_{\rm CO} = 0.8\,M_{\odot}/({\rm K\,km\,s^{-1}\,pc^2})$ as justified in Sect. 9.

We find that all sources fall closer to the upper "starburst" than the lower "main sequence" lines in Fig. 10. To illustrate the effects of lensing, i.e., how these sources might appear in the image plane, we plot not only the observed luminosities (red filled stars), but also the luminosities for fiducial magnification factors $\mu = 10$ and $\mu = 50$ (orange and light blue empty stars in Fig. 10). Even without the detailed lens modelling their position in the diagram relative to typical starburst or main-sequence galaxies does not depend sensitively on the precise magnification factor.

We stress that in the present study, we only show integrated measurements, whereas the relationship that underlies the Schmidt-Kennicutt diagram is between the surface density of molecular gas mass and the star-formation rate. Our on-going interferometric follow-up programme will enable us to derive more detailed constraints, and to investigate whether the "starburst" and "main sequence" classifications are unique for each source, or whether each individual Dusty GEM will show a range in star-formation efficiency.

FIR luminosities and gas mass estimates also provide simple, rough constraints on the gas depletion timescale, $t_{\rm dpl} = M_{\rm gas}/{\rm SFR}$, and hence the time during which the current star formation intensity can be maintained without replenishing the molecular gas reservoirs. Assuming that star-formation rates are constant, we find short gas depletion timescales, $t_{\rm dpl} = (0.5{-}6)\times 10^7$ yr, significantly less than the typical stellar age of a FIR or sub-mm galaxy (a few times 10^8 yr, Smail et al. 2004; Lapi et al. 2012), and also somewhat, but not dramatically, shorter than the gas depletion timescales found for unlensed sub-mm galaxies (e.g., Greve et al. 2005). This highlights again the fact that our sources have all the hallmarks of being "ordinary" dusty starburst galaxies placed under particularly powerful cosmic microscopes.

11. Summary

We have presented a first analysis of an extensive multi-wavelength follow-up campaign of a new sample of the brightest high-redshift FIR and sub-mm galaxies, discovered through the unique synergy of the *Planck* and *Herschel* satellites. *Planck*'s all-sky nature and multi-frequency coverage allows us to select rare peaks in the sub-mm background and *Herschel* observations lead to subsample of strongly lensed candidates – *Planck*'s Dusty GEMS. Their FIR peak flux densities are up to $S_{350} = 1130$ mJy at 350 μm, including six sources that are above the completeness limit of *Planck* at the highest frequencies. Our sample extends the very successful searches for gravitationally lensed high-z galaxies already carried out with *Herschel* and the SPT towards the brightest, rarest targets on the FIR and sub-mm sky, which emphasized the need for a genuine all-sky survey to systematically probe such exceedingly uncommon sources.

All sources in our sample are bright, isolated point sources in SPIRE 250-μm maps (18″ FWHM), and have the typical FIR-to-mm SEDs of dusty, intensely star-forming galaxies at high redshift. They have redshifts in the range $z = 2.2$–3.6, based on multiple bright millimetre emission lines obtained with EMIR at the IRAM 30-m telescope. Their dust and gas properties provide firm evidence that they are indeed gravitationally lensed galaxies, as is further supported through interferometric observations of their dust and gas morphologies, already obtained for most sources.

We used the WISE survey at 22 μm and the 1.4 GHz VLA FIRST survey to show that the FIR continuum of the Dusty GEMS is not dominated by the radiation of powerful AGN. In particular, we find that buried quasars cannot make a dominant contribution to their observed FIR SEDs. All SEDs are well fitted with a single modified blackbody distribution with temperatures $T_{\rm d} = 33$–50 K, covering the range of high-redshift starburst galaxies, as well as more gradually, but still intensely star-forming, high-z galaxies on the "main sequence". They show a wide scatter about the local FIR radio correlation, with q-parameters ranging from 2.0, as has previously been found for high-z galaxies by some authors, to above 2.7, which suggests a considerable excess of FIR relative to synchrotron emission. One plausible interpretation is that this is probably a consequence of their turbulent ISM, but this needs to be confirmed through more detailed studies comparing the resolved radio emission with other source properties. All galaxies have gas-to-dust ratios of 40–140, consistent with a low CO-to-H_2 conversion factor, as expected for massive, dusty starburst galaxies with metallicities above solar. A full analysis of the spatially resolved properties of these galaxies, as well as detailed lens modelling, is on-going.

Strongly lensed high-redshift sub-mm galaxies represent an excellent opportunity to study gas heating and acceleration, and the mechanism driving star formation in the most vigorous starbursts in the early Universe. Detailed observations of the dust, stellar populations, and multiple emission and absorption lines, in particular with sub-mm and millimetre interferometry have already been obtained and will be discussed in future papers.

Acknowledgements. We would like to thank the staff at the IRAM 30-m telescope, in particular N. Billot and S. Trevino, for their excellent support during observations. We are also very grateful to the former director of IRAM, P. Cox, the director of the SMA, R. Blundell, the director of the CFHT, D. Simons, and the director of ESO, T. de Zeeuw, for the generous allocation of Director's Discretionary Time. We thank the referee, S. Bussmann, for constructive comments that helped improve our manuscript. We would also like to thank A. Sajina and several other colleagues unknown to us and sollicited by the Planck collaboration as external referees for their valuable comments on an earlier version of the paper. We would also like to thank C. Kramer for having made his CLASS routine FTSPlatformingCorrection5 available to us. We thank B. Partridge and the Planck Editorial Board for ensuring that our manuscript is in accordance with the internal Planck publication rules and standards. R.C. wishes to acknowledge support from the École Doctorale Astronomie & Astrophysique de l'Île de France. M.N. acknowledges financial support from ASI/INAF agreement 2014-024-R.0 and from PIRN-INAF 2012 project "Looking into the dust-obscured phase of galaxy formation through cosmic zoom lenses in the *Herschel* Astrophysical Large Area Survey". I.F.C., L.M. and E.P. acknowledge the support of grant ANR-11-BS56-015. The largest part of this work is based on observations carried out with the IRAM 30-m Telescope and the IRAM Plateau de Bure Interferometer. IRAM is supported by INSU/CNRS (France), MPG (Germany) and IGN (Spain). The Submillimeter Array is a joint project between the Smithsonian Astrophysical Observatory and the Academia Sinica Institute of Astronomy and Astrophysics and is funded by the Smithsonian Institution and the Academia Sinica. Based in part on observations obtained with MegaPrime/MegaCam, a joint project of CFHT and CEA/DAPNIA, at the Canada-France-Hawaii Telescope (CFHT), which is operated by the National Research Council (NRC) of Canada, the Institute National des Sciences de l'Univers of the Centre National de la Recherche Scientifique of France, and the University of Hawaii. Based in part on observations obtained with WIRCam, a joint project of CFHT, Taiwan, Korea, Canada, France, and the Canada-France-Hawaii Telescope (CFHT). The development of *Planck* has been supported by: ESA; CNES and CNRS/INSU-IN2P3-INP (France); ASI, CNR, and INAF (Italy); NASA and DoE (USA); STFC and UKSA (UK); CSIC, MICINN, JA, and RES (Spain); Tekes, AoF, and CSC (Finland); DLR and MPG (Germany); CSA (Canada); DTU Space (Denmark); SER/SSO (Switzerland); RCN (Norway); SFI (Ireland); FCT/MCTES (Portugal); and PRACE (EU). A description of the Planck Collaboration and a list of its members, including the technical or scientific activities in which they have been involved, can be found at[4]. The *Herschel* spacecraft was designed, built, tested, and launched under a contract to ESA managed by the *Herschel*/*Planck* Project team by an industrial consortium under the overall responsibility of the prime contractor Thales Alenia Space (Cannes), and including Astrium (Friedrichshafen) responsible for the payload module and for system testing at spacecraft level, Thales Alenia Space (Turin) responsible for the service module, and Astrium (Toulouse) responsible for the telescope, with in excess of a hundred subcontractors. We acknowledge the use of the Galaxies, INterstellar mater & COsmology (GINCO) archive for the Integrated Data & Operation Centre (IDOC) at Institut d'Astrophysique Spatiale and Observatoire des Sciences de l'Univers de l'Université Paris Sud (OSUPS). Support for IDOC is provided by CNRS & CNES.

References

Alexander, D. M., Bauer, F. E., Chapman, S. C., et al. 2005, ApJ, 632, 736
Armus, L., Charmandaris, V., Bernard-Salas, J., et al. 2007, ApJ, 656, 148
Baugh, C. M., Lacey, C. G., Frenk, C. S., et al. 2005, MNRAS, 356, 1191
Becker, R. H., White, R. L., & Helfand, D. J. 1995, ApJ, 450, 559
Bertin, E. 2010a, SCAMP: Automatic Astrometric and Photometric Calibration, Astrophysics Source Code Library [record ascl:1010.063]
Bertin, E. 2010b, SWarp: Resampling and Co-adding FITS Images Together, Astrophysics Source Code Library [record ascl:1010.068]
Béthermin, M., Daddi, E., Magdis, G., et al. 2012, ApJ, 757, L23
Blain, A. W., Barnard, V. E., & Chapman, S. C. 2003, MNRAS, 338, 733
Bothwell, M. S., Smail, I., Chapman, S. C., et al. 2013, MNRAS, 429, 3047
Bourne, N., Dunne, L., Ivison, R. J., et al. 2011, MNRAS, 410, 1155
Brandl, B. R., Bernard-Salas, J., Spoon, H. W. W., et al. 2006, ApJ, 653, 1129
Bressan, A., Silva, L., & Granato, G. L. 2002, A&A, 392, 377
Bussmann, R. S., Pérez-Fournon, I., Amber, S., et al. 2013, ApJ, 779, 25
Chapin, E. L., Berry, D. S., Gibb, A. G., et al. 2013, MNRAS, 430, 2545
Chapman, S. C., Blain, A. W., Smail, I., & Ivison, R. J. 2005, ApJ, 622, 772
Combes, F., Rex, M., Rawle, T. D., et al. 2012, A&A, 538, L4
Condon, J. J. 1992, ARA&A, 30, 575
Daddi, E., Elbaz, D., Walter, F., et al. 2010, ApJ, 714, L118
Danielson, A. L. R., Swinbank, A. M., Smail, I., et al. 2011, MNRAS, 410, 1687
Dekel, A., Sari, R., & Ceverino, D. 2009, ApJ, 703, 785
Dempsey, J. T. Friberg, P., Jenness, T., et al. 2013, MNRAS, 430, 2534
Diolaiti, E., Bendinelli, O., Bonaccini, D., et al. 2000, A&AS, 147, 335
Dole, H., Lagache, G., Puget, J.-L., et al. 2006, A&A, 451, 417
Downes, D., & Solomon, P. M. 1998, ApJ, 507, 615
Drouart, G., De Breuck, C., Vernet, J., et al. 2014, A&A, 566, A53
Egami, E., Rex, M., Rawle, T. D., et al. 2010, A&A, 518, L12
Elbaz, D., Dickinson, M., Hwang, H. S., et al. 2011, A&A, 533, A119
Fiolet, N., Omont, A., Lagache, G., et al. 2010, A&A, 524, A33
Förster Schreiber, N. M., Genzel, R., Bouché, N., et al. 2009, ApJ, 706, 1364
Fu, H., Jullo, E., Cooray, A., et al. 2012, ApJ, 753, 134
Genzel, R., Tacconi, L. J., Gracia-Carpio, J., et al. 2010, MNRAS, 407, 2091
Genzel, R., Tacconi, L. J., Combes, F., et al. 2012, ApJ, 746, 69
Gildas Team. 2013, GILDAS: Grenoble Image and Line Data Analysis Software, astrophysics Source Code Library [record ascl:1305.010]
Glover, S. C. O., & Mac Low, M.-M. 2011, MNRAS, 412, 337
Greve, T. R., Bertoldi, F., Smail, I., et al. 2005, MNRAS, 359, 1165
Greve, T. R., Vieira, J. D., Weiß, A., et al. 2012, ApJ, 756, 101
Harris, A. I., Baker, A. J., Frayer, D. T., et al. 2012, ApJ, 752, 152
Hauser, M. G., & Dwek, E. 2001, ARA&A, 39, 249
Herranz, D., González-Nuevo, J., Clements, D. L., et al. 2013, A&A, 549, A31
Holland, W. S., Bintley, D., Chapin, E. L., et al. 2013, MNRAS, 430, 2513
Ivison, R. J., Alexander, D. M., Biggs, A. D., et al. 2010a, MNRAS, 402, 245
Ivison, R. J., Magnelli, B., Ibar, E., et al. 2010b, A&A, 518, L31
Ivison, R. J., Swinbank, A. M., Smail, I., et al. 2013, ApJ, 772, 137
Jarvis, M. J., Smith, D. J. B., Bonfield, D. G., et al. 2010, MNRAS, 409, 92
Kennicutt, Jr., R. C. 1998, ARA&A, 36, 189
Kovacs, A. 2013, CRUSH: Comprehensive Reduction Utility for SHARC-2, astrophysics Source Code Library [record ascl:1308.011]
Kovács, A., Chapman, S. C., Dowell, C. D., et al. 2006, ApJ, 650, 592
Lacki, B. C., & Thompson, T. A. 2010, ApJ, 717, 196
Laird, E. S., Nandra, K., Pope, A., & Scott, D. 2010, MNRAS, 401, 2763
Lapi, A., Negrello, M., González-Nuevo, J., et al. 2012, ApJ, 755, 46
Lehnert, M. D., Nesvadba, N. P. H., Le Tiran, L., et al. 2009, ApJ, 699, 1660
Lehnert, M. D., Le Tiran, L., Nesvadba, N. P. H., et al. 2013, A&A, 555, A72
Leroy, A. K., Walter, F., Brinks, E., et al. 2008, AJ, 136, 2782
Magdis, G. E., Daddi, E., Elbaz, D., et al. 2011, ApJ, 740, L15
Michałowski, M., Hjorth, J., & Watson, D. 2010, A&A, 514, A67
Moshir, M., Kopman, G., & Conrow, T. A. O. 1992, IRAS Faint Source Survey, Explanatory supplement version 2
Mullaney, J. R., Alexander, D. M., Goulding, A. D., & Hickox, R. C. 2011, MNRAS, 414, 1082
Murphy, E. J. 2009, ApJ, 706, 482
Narayanan, D., Krumholz, M. R., Ostriker, E. C., & Hernquist, L. 2012, MNRAS, 421, 3127
Negrello, M., Perrotta, F., González-Nuevo, J., et al. 2007, MNRAS, 377, 1557
Negrello, M., Hopwood, R., De Zotti, G., et al. 2010, Science, 330, 800
Nenkova, M., Sirocky, M. M., Nikutta, R., Ivezić, Ž., & Elitzur, M. 2008, ApJ, 685, 160
Nesvadba, N. P. H., Lehnert, M. D., Genzel, R., et al. 2007, ApJ, 657, 725
Nguyen, H. T., Schulz, B., Levenson, L., et al. 2010, A&A, 518, L5
Omont, A. 2007, Rep. Prog. Phys., 70, 1099
Planck Collaboration VII. 2011, A&A, 536, A7
Planck Collaboration I. 2014, A&A, 571, A1
Planck Collaboration VI. 2014, A&A, 571, A6
Planck Collaboration XXVIII. 2014, A&A, 571, A28
Planck Collaboration Int. XXVII. 2015, in press, DOI: 10.1051/0004-6361/201424790
Polletta, M., Tajer, M., Maraschi, L., et al. 2007, ApJ, 663, 81
Rawle, T. D., Egami, E., Bussmann, R. S., et al. 2014, ApJ, 783, 59
Sajina, A., Yan, L., Lacy, M., & Huynh, M. 2007, ApJ, 667, L17
Sajina, A., Yan, L., Fadda, D., Dasyra, K., & Huynh, M. 2012, ApJ, 757, 13
Sargent, M. T., Schinnerer, E., Murphy, E., et al. 2010, ApJ, 714, L190
Schmidt, M. 1959, ApJ, 129, 243
Serjeant, S. 2012, MNRAS, 424, 2429
Silk, J., & Norman, C. 2009, ApJ, 700, 262
Smail, I., Chapman, S. C., Blain, A. W., & Ivison, R. J. 2004, ApJ, 616, 71
Solomon, P. M., & Vanden Bout, P. A. 2005, ARA&A, 43, 677
Solomon, P. M., Downes, D., Radford, S. J. E., & Barrett, J. W. 1997, ApJ, 478, 144
Soucail, G., Fort, B., Mellier, Y., & Picat, J. P. 1987, A&A, 172, L14
Staguhn, J. G., Benford, D. J., Fixsen, D. J., et al. 2012, in SPIE Conf. Ser., 8452
Swinbank, A. M., Chapman, S. C., Smail, I., et al. 2006, MNRAS, 371, 465
Swinbank, A. M., Smail, I., Longmore, S., et al. 2010, Nature, 464, 733
Swinbank, A. M., Papadopoulos, P. P., Cox, P., et al. 2011, ApJ, 742, 11
Tabatabaei, F. S., Schinnerer, E., Murphy, E. J., et al. 2013, A&A, 552, A19
Thomson, A. P., Ivison, R. J., Simpson, J. M., et al. 2014, MNRAS, 442, 577
Vieira, J. D., Marrone, D. P., Chapman, S. C., et al. 2013, Nature, 495, 344

[4] http://www.rssd.esa.int/index.php?project=PLANCK&page=Planck_Collaboration

Vlahakis, C., Eales, S., & Dunne, L. 2007, MNRAS, 379, 1042
Walsh, D., Carswell, R. F., & Weymann, R. J. 1979, Nature, 279, 381
Wardlow, J. L., Cooray, A., De Bernardis, F., et al. 2013, ApJ, 762, 59
Weiß, A., De Breuck, C., Marrone, D. P., et al. 2013, ApJ, 767, 88
Yan, L., Donoso, E., Tsai, C.-W., et al. 2013, AJ, 145, 55

[1] Institut d'Astrophysique Spatiale, UMR 8617, Université Paris-Sud, Bât. 121, 91405 Orsay, France
[2] CNRS, 91405 Orsay, France
[3] Institut Universitaire de France, Paris, France
[4] Department of Physics & Astronomy, University of British 66 Columbia, 6224 Agricultural Road, Vancouver, British Columbia, 58 Canada
[5] Institut de Radio Astronomie Millimétrique (IRAM), 300 rue de la Piscine, Domaine Universitaire, 38406 Saint-Martin d'Hères, France
[6] Harvard-Smithsonian Center for Astrophysics, Cambridge, MA 02138, USA
[7] Steward Observatory, University of Arizona, Tucson, AZ 85721, USA
[8] Université de Toulouse, UMS-OMP, IRAP, 31028 Toulouse Cedex 4, France
[9] CNRS, IRAP, 9 Av. colonel Roche, BP 44346, 31028 Toulouse Cedex 4, France
[10] INAF, Osservatorio Astronomico di Padova, Vicolo dell'Osservatorio 5, 35122 Padova, Italy
[11] CEA-Saclay, 91191 Gif-sur-Yvette, France
[12] Aix-Marseille Université, CNRS, LAM (Laboratoire d'Astrophysique de Marseille) UMR 7326, 13388 Marseille, France
[13] ESAC, ESA, PO Box 78, Villanueva de la Cañada, 28691 Madrid, Spain
[14] Infrared Processing and Analysis Center, California Institute of Technology, Pasadena, CA 91125, USA
[15] European Southern Observatory, Karl-Schwarzschild Str. 2, 85748 Garching, Germany
[16] European Southern Observatory, ESO Vitacura, Alonso de Cordova 3107, Vitacura, Casilla 19001, Santiago, Chile
[17] Atacama Large Millimeter/submillimeter Array, ALMA Santiago Central Offices, Alonso de Cordova 3107, Vitacura, Casilla 763-0355, Santiago, Chile
[18] School of Earth and Space Exploration, Arizona State University, Tempe, AZ 85287, USA
[19] UPMC Univ. Paris 06, UMR 7095, Institut d'Astrophysique de Paris, 75014 Paris, France
[20] Department of Physics, University of Oxford, Denys Wilkinson Building, Keble Road, Oxford OX1 3RH, UK